

## THE INNER KILOPARSEC OF MRK 273 WITH KECK ADAPTIVE OPTICS

VIVIAN U<sup>1,9</sup>, ANNE MEDLING<sup>2</sup>, DAVID SANDERS<sup>1</sup>, CLAIRE MAX<sup>2</sup>, LEE ARMUS<sup>3</sup>, KAZUSHI IWASAWA<sup>4</sup>, AARON EVANS<sup>5,6</sup>, LISA KEWLEY<sup>1,7</sup>, GIOVANNI FAZIO<sup>8</sup>

*Draft version July 3, 2018*

### ABSTRACT

There is X-ray, optical, and mid-infrared imaging and spectroscopic evidence that the late-stage ultraluminous infrared galaxy merger Mrk 273 hosts a powerful AGN. However, the exact location of the AGN and the nature of the nuclei have been difficult to determine due to dust obscuration and the limited wavelength coverage of available high-resolution data. Here we present near-infrared integral-field spectra and images of the nuclear region of Mrk 273 taken with OSIRIS and NIRC2 on the Keck II Telescope with laser guide star adaptive optics. We observe three spatially-resolved components, and analyze the local molecular and ionized gas emission lines and their kinematics. We confirm the presence of the hard X-ray AGN in the southwest nucleus. In the north nucleus, we find a strongly-rotating gas disk whose kinematics indicate a central black hole of mass  $1.04 \pm 0.1 \times 10^9 M_{\odot}$ . The H<sub>2</sub> emission line shows an increase in velocity dispersion along the minor axis in both directions, and an increased flux with negative velocities in the southeast direction; this provides direct evidence for a collimated molecular outflow along the axis of rotation of the disk. The third spatially-distinct component appears to the southeast, 640 and 750 pc from the north and southwest nuclei, respectively. This component is faint in continuum emission but shows several strong emission line features, including [Si VI] 1.964  $\mu\text{m}$  which traces an extended coronal line region. The geometry of the [Si VI] emission combined with shock models and energy arguments suggest that [Si VI] in the southeast component must be at least partly ionized by the SW AGN or a putative AGN in the northern disk, either through photoionization or through shock-heating from strong AGN- and circumnuclear starburst-driven outflows. This lends support to a scenario in which Mrk 273 may be a dual AGN system.

*Subject headings:* galaxies: active — galaxies: interactions — galaxies: individual (Mrk 273) — galaxies: kinematics and dynamics — galaxies: nuclei

### 1. INTRODUCTION

When gas-rich galaxies collide and merge, gaseous material can lose angular momentum and funnel toward the center of the merger system (e.g. Barnes & Hernquist 1992). There it can feed starburst and active galactic nuclei (AGN) activities which power luminous and ultraluminous infrared galaxies ((U)LIRGs). The detailed processes of how merger dynamics contribute to AGN activity (Sanders et al. 1988; Hopkins et al. 2006; Comerford et al. 2009), how mass builds up in the central supermassive black hole (Hopkins et al. 2010; Treister et al. 2010; Rosario et al. 2011), how much

energy is deposited into the system by the ionizing sources (Younger et al. 2009; Sanders & Mirabel 1996), and when the active nuclei are triggered (Donley et al. 2010; Hopkins 2012; Farrah et al. 2009) are areas of active research. Because AGN have been observed in mergers with double nuclei (Komossa et al. 2003; Ballo et al. 2004; Koss et al. 2012; Fu et al. 2011; Liu et al. 2011; McGurk et al. 2011; Gerke et al. 2007; Mazzarella et al. 2012), it is known that an AGN can “turn on” before the final coalescence of the nuclei. However, many mergers do not host dual AGN (e.g. Teng et al. 2012). It is inconclusive from the models when an AGN is triggered and what dictates whether or not synchronous ignition occurs (Van Wassenhove et al. 2012).

These questions can be addressed with high-resolution observations of the nuclei in nearby luminous infrared galaxy mergers. Previous integral-field spectroscopic work on large samples of (U)LIRGs have mapped the large-scale distribution and kinematics of ionized gas, compared them to that of stellar components, determined metallicity gradients, and found evidence for galactic outflows and shocks (e.g. Westmoquette et al. 2012; Rich et al. 2011, 2012; García-Marín et al. 2009). Much of the gas is concentrated within the dusty cores of these (U)LIRGs, so longer wavelengths must be probed to understand the nuclear regions. Piqueras López et al. (2012) has presented an atlas of the 2D molecular and ionized gas structure in the southern local (U)LIRGs as probed in the near-infrared, showing the extent and kinematics of the gaseous components at  $\sim 0.2$  and  $0.9$

<sup>1</sup> Institute for Astronomy, University of Hawaii, 2680 Woodlawn Dr., Honolulu, HI 96822, USA

<sup>2</sup> Department of Astronomy and Astrophysics, University of California, Santa Cruz, 1156 High Street, Santa Cruz, CA 95064, USA

<sup>3</sup> Spitzer Science Center, California Institute of Technology, 1200 E. California Blvd., Pasadena, CA 91125, USA

<sup>4</sup> ICREA and Institut del Ciències del Cosmos, Universitat de Barcelona (IEEC-UB), Martí i Franquès, 1, E-08028 Barcelona, Spain

<sup>5</sup> Department of Astronomy, University of Virginia, 530 McCormick Road, Charlottesville, VA 22904, USA

<sup>6</sup> National Radio Astronomy Observatory, 520 Edgemont Road, Charlottesville, VA 22903, USA

<sup>7</sup> Research School for Astronomy and Astrophysics, Australian National University, Cotter Road, Weston Creek, ACT 2611, Australia

<sup>8</sup> Harvard-Smithsonian Center for Astrophysics, 60 Garden St., Cambridge, MA 02138, USA

<sup>9</sup> *Current Address:* Department of Physics and Astronomy, University of California, Riverside, 900 University Avenue, Riverside, CA 92521, USA; vivianu@ucr.edu

kpc spatial resolution. These seeing-limited observations with an average angular resolution of  $\sim 0''.63$  full-width half-maximum (FWHM) set the framework of the large kiloparsec-scale conditions of the gas and prompt detailed high-resolution investigations of the nuclear regions.

Due to the advent of laser guide star adaptive optics (LGS AO; Wizinowich et al. 2006; van Dam et al. 2006), black holes in local (U)LIRGs can now be examined at the subarcsecond level (Max et al. 2007; Melbourne et al. 2008; Engel et al. 2010; Davies et al. 2010; Medling et al. 2011). In particular, the OH-Suppressing Infra-Red Imaging Spectrograph (OSIRIS; Larkin et al. 2006), an integral-field unit (IFU) with near-infrared wavelength coverage ( $1\mu\text{m} < \lambda < 2.4\mu\text{m}$ ) on the Keck II telescope, offers imaging and kinematic information at  $< 0''.1$  spatial resolution with LGS AO (e.g. Wright et al. 2009; Law et al. 2009; Do et al. 2009; McConnell et al. 2011; Walsh et al. 2012). NIRC2 (PIs: Keith Matthews and Tom Soifer), a diffraction-limited infrared camera also on the Keck II telescope, offers scales of  $\sim 0.01''/\text{pixel}$  in the  $1 - 5\mu\text{m}$  range in its narrow camera mode. They both probe the near-infrared regime where dust extinction does not pose as severe a problem.

To understand the mechanisms responsible for powering the extreme infrared luminosities in (U)LIRGs, we are conducting a survey of nearby galaxy mergers using OSIRIS to probe the gas kinematics and energetics of the nuclear regions in these systems. Observed as part of the larger campaign, Mrk 273 (= UGC 08696) is the focus of this paper as an advanced merger with infrared luminosity  $L_{\text{IR}} = 10^{12.21} L_{\odot}$ . At a distance of  $z = 0.038$  (systemic velocity  $cz = 11,400 \text{ km s}^{-1}$ ; physical scale =  $0.754 \text{ kpc}''^{10}$ ), it exhibits a prominent optical tidal tail ( $\sim 40 \text{ kpc}$ ) extending to the south (Fig. 1). With its high infrared luminosity, this ULIRG has a heated dusty core that obscures the central ionizing sources in optical light. As one of the brightest and closest ULIRGs, Mrk 273 has been well-studied across the full wavelength spectrum, including *Spitzer*, *Hubble*, *Chandra*, and *GALEX* observations from the Great Observatories All-sky LIRG Survey (GOALS; Armus et al. 2009; Howell et al. 2010; Iwasawa et al. 2011b). However, the details of its power engine remain controversial.

There is substantial evidence in the literature suggesting that at least one AGN resides within Mrk 273: Armus et al. (2007) detected the [Ne V] line in *Spitzer's* mid-infrared IRS spectrum, and measured hot gas with  $T > 300\text{K}$  in the continuum. Polycyclic aromatic hydrocarbon strength diagnostics from mid-infrared Infrared Space Observatory spectroscopy classify the galaxy as an AGN (Lutz et al. 1999; Rigopoulou et al. 1999). Hard X-ray emission and the Fe K line (e.g. Xia et al. 2002; Iwasawa et al. 2011a; Ptak et al. 2003) have also been detected in support of the presence of a hard X-ray AGN, though most of the total power is likely to be from circumnuclear starbursts (Iwasawa et al. 2011a).

The status of Mrk 273 as a ULIRG and a late-stage pre-coalescence merger makes it an important galaxy for

understanding the role of mergers in galaxy evolution. The specific goals of our high-resolution IFU study are to locate the nuclei of the progenitor galaxies, to determine the characteristics of any supermassive black holes, to verify their active or dormant nature, and to investigate the relative effect of AGN activity and star formation on the surrounding nuclear regions.

Multiwavelength studies have decomposed the nuclear region into multiple components. Three main components have been identified from the detected radio continuum: north, southeast, and southwest (N, SE, SW; Condon et al. 1991; Smith et al. 1998) as indicated in Fig. 1. These components show dissimilar characteristics in most bands; it is not clear which of them may be remnant nuclei. We combine our data with existing evidence to determine the likely sources of each. The SE emission is only weakly detected in the near-infrared (Scoville et al. 2000) and weak or undetectable in the X-ray given the limited resolution of *Chandra* (Iwasawa et al. 2011a), but the N and SW X-ray emission coincide with peaks in the near-infrared continuum flux. OH maser emission along with steep radio spectral index suggest the presence of a low-luminosity AGN with a binding mass of  $1.39 \pm 0.16 \times 10^9 M_{\odot}$  in the N component (Klöckner & Baan 2004). The N radio-1.4GHz emission is further resolved into individual compact sources thought to be clustered supernovae (Smith et al. 1998; Carilli & Taylor 2000; Bondi et al. 2005). More recently, Iwasawa et al. (2011a) found, in *Chandra* images with improved astrometry, that the hard X-ray flux is superposed on the SW compact source, with a 6-7keV excess extending toward the north. They determined that the known hard X-ray AGN is located at the SW component, and attributed the 6–7 keV excess to enhanced Fe K emission either from the SW source or from a heavily absorbed Compton-thick AGN at the N component.

In this paper, we present high-resolution infrared integral-field spectroscopy and imaging observations of Mrk 273 taken with the OSIRIS and NIRC2 instruments on the Keck II Telescope, probing down to the  $\leq 0''.1$  scale. These near-infrared high-resolution maps provide great detail for identifying the location of the hardest photons from AGN and shocks as well as the dynamics of the gas. Observations and data processing are described in §2. Resulting spectra and images are analyzed and presented in §3 and §4; our interpretations are detailed in §5. Our conclusions are summarized in §6. We adopt  $H_0 = 70 \text{ km s}^{-1} \text{ Mpc}^{-1}$ ,  $\Omega_m = 0.28$ , and  $\Omega_{\Lambda} = 0.72$  throughout the paper.

## 2. OBSERVATIONS AND DATA REDUCTION

### 2.1. OSIRIS Data Cubes

The Keck OSIRIS observations were obtained on UT 2011 May 22 under clear, dry, and stable conditions with the LGS AO system. Two filter-scale combinations were used to observe Mrk 273: the broad *K*-band filter ( $\lambda = 1965 - 2381\text{nm}$ ; hereafter Kcb) at the 100mas/pixel scale ( $\sim 75\text{pc}$  for Mrk 273), and a narrow *H*-band filter ( $\lambda = 1652 - 1737\text{nm}$ ; hereafter Hn4) at the 35mas/pixel scale ( $\sim 26\text{pc}$  for Mrk 273). The tip-tilt star employed for the AO corrections had *R* magnitude  $m_R = 16.1$  at  $33''$  away from the target, well within the LGS requirement constraints. We adopted a position angle of  $30^\circ$  East of

<sup>10</sup> Physical scale has been computed with a cosmology calculator (Wright 2006).

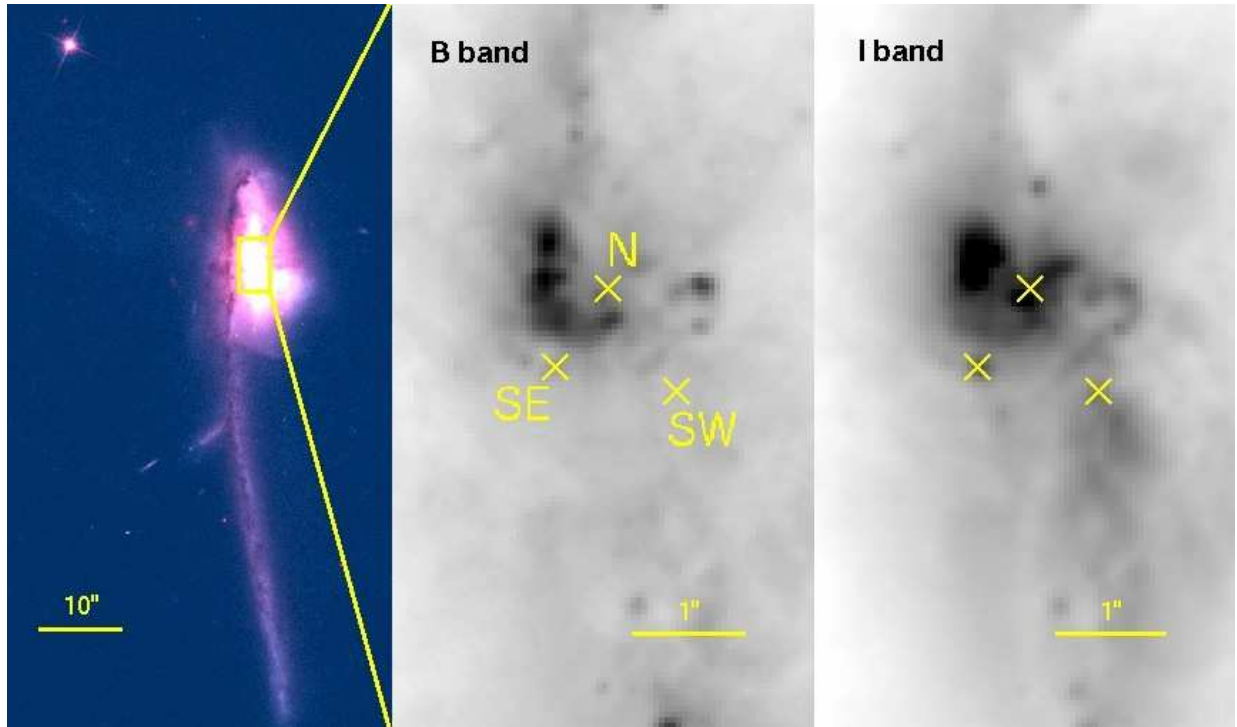


FIG. 1.— (Left) *HST* ACS  $B(F435W) + I(F814W)$  composite image of Mrk 273. In these and subsequent images, north is up and east is to the left. The box indicates the zoomed in region in the grey-scale panels. (Middle) and (right) are the zoomed in  $B$ - and  $I$ -band images, respectively. The three crosses mark the N, SE, and SW sources of interest identified in radio observations (Carilli & Taylor 2000; Bondi et al. 2005) whose near-infrared characteristics will be presented in this paper.

North and an observing scheme of object-sky-object with 10-minute integration per frame, totaling 50-minute and 60-minute on-source times for the Kcb-100mas and Hn4-35mas observations, respectively. The A0V star 81 UMa was observed at 2 different airmasses in the Kcb filter (3 in Hn4) for telluric corrections.

The data sets were processed using the OSIRIS pipeline version 2.3 (Krabbe et al. 2004). The full Astronomical Reduction Pipeline template (ARP\_SPEC) incorporates dark-frame subtraction, channel level adjustment, crosstalk removal, glitch identification, cosmic ray cleaning, spectra extraction for data cube assembly, dispersion correction, scaled sky subtraction for enhanced OH-line suppression, and telluric correction. The extracted spectra were subsequently cleaned to remove bad pixels. The cleaned frames were registered using the SW peak position and combined using the pipeline’s clipped mean algorithm. The final data cubes encompass signal at each pixel in the  $x$ ,  $y$ , and wavelength dimensions. The FWHM of the tip-tilt star was  $0''.05$  in the Kcb setting and  $0''.06$  in the Hn4 setting.

The final OSIRIS Kcb and Hn4 cubes have been flux-calibrated to the respective  $K'$ - and  $H$ -band NIRC2 flux-calibrated images (see §2.2) in the following manner. Spatially-coincident regions were first defined within resolution uncertainties in the OSIRIS and NIRC2 images of the matching bands. Spectroscopically, the bandwidth differences between the OSIRIS data cubes and the NIRC2 images have been taken into account while integrating over the Kcb and Hn4 wavelength ranges, respectively. Conversion factors thus determined offer a calibration to absolute fluxes in physical units that allow for line ratio computations across the two bands.

It is important to understand the point-spread func-

tion (PSF) intrinsic to our OSIRIS observations before comparing them to models. We estimate our PSF by fitting a Moffat profile to images of the tip-tilt star taken right before our galaxy observation sets. However, this is a best-case limit for the PSF, because the AO correction will degrade somewhat when moving off-axis to the galaxy. The tip-tilt star provides low-order corrections, which vary on scales of the isokinetic angle. (This angle is much larger than the isoplanatic angle, which governs how wide a field-of-view a laser guide star can correct.) At Mauna Kea, the isokinetic angle is approximately  $75''$  (van Dam et al. 2006); this represents the tip-tilt star distance at which Strehl will be degraded by  $1/e$ . Because our tip-tilt star is at a separation of  $\sim 33''$  from Mrk 273, we expect our Strehl to be degraded by a factor of  $\sim 0.6$  from the tip-tilt star profile. To model this, we convolve our tip-tilt star PSF model by a Gaussian of FWHM  $0''.05$  to estimate our true PSF.

## 2.2. NIRC2 Images

High-resolution images were also obtained with NIRC2, using the narrow camera mode ( $0''.009942$  pixel $^{-1}$ ;  $8$  pc pixel $^{-1}$ ) and the LGS AO System, on UT 2012 May 20. Images were taken in the  $H$ - ( $\lambda_c = 1633$  nm) and  $K'$ - ( $\lambda_c = 2124$  nm) bands, with exposure times of 9 minutes each. Individual frames were exposed for 30 seconds for each of two coadds; frames were dithered using the standard ‘bxy3’ dither pattern that avoids the noisy lower-left quadrant of the chip. The same tip-tilt star used in the OSIRIS observations was used here. We reduced our images using the CfAO Treasury Survey pipeline (Glassman et al. 2002; Melbourne et al. 2005). A sky frame was produced by combining sky regions of each dithered frame, then subtracted from each frame. A

flat field was created by normalizing the constructed sky frame. This flat field was then divided out of each frame in order to correct for varying sensitivities across the detector. The sky-subtracted-and-flattened images were subsequently aligned and median-combined to obtain the final reduced image, which were then flux-calibrated using images taken of the UKIRT Faint Standard star FS 133 (Hawarden et al. 2001). Standard star exposures were 5 seconds per frame, also dithered with the ‘bxy3’ script; four frames were combined for the  $H$ -band standard, three for the  $K'$ -band standard. A FWHM of  $\sim 0''.06$  has been measured from a compact source south of the SE component in both the  $H$ - and  $K'$ -band images.

### 3. EMISSION LINE FITTING AND ERROR ANALYSIS

From each of the reduced OSIRIS Kcb and Hn4 data cubes, various emission lines were mapped as follows. First we extracted the continuum with power-law fits and subtracted it from the spectrum. We measured the signal-to-noise (S/N) ratio of the lines of interest based on the line flux and root-mean-square (rms) residuals of the continuum. We fit the lines with a Gaussian profile to determine the flux, velocity (shift from the systemic velocity,  $11,400 \text{ km s}^{-1}$ ), and velocity dispersion (sigma of the Gaussian). In order to gauge the accuracy of the line-fit parameters, synthetic data cubes were then generated using the line parameters fitted to each pixel. The S/N ratio measured above determined the random noise level added to the synthetic cube. We then refit the line parameters of the synthetic cube 500 times with random noise added. The final uncertainty in each parameter’s original measurement was obtained from the distribution of that of the resulting models.

We adopted this procedure for each line species. Different lines are treated separately from each other, but all the  $\text{H}_2$  transitions or both the  $\text{Br}\gamma$  and  $\text{Br}\delta$  lines are fitted simultaneously. An example of the simultaneous fit of the  $\text{H}_2$  transitions for a typical pixel in the Kcb cube is shown in Fig. 2. Visual inspection ensured that the line fits were sensible with appropriate continuum levels determined within each spectral window. We noted that in many of the pixels with [Si VI] detection, the fit of a single Gaussian profile resulted in large residuals. In such cases we fit a broad and a narrow Gaussian component to these lines; this significantly improved the residuals (Fig. 3). The pixels associated with the two components appeared to be spatially segregated. The physical implication of this double-component fit is further discussed in §4.2.4.

In order to increase the S/N ratio for regions with inadequate flux, we adopted optimal Voronoi binning for the investigation of the kinematics using the Cappellari & Copin (2003) code. This algorithm bins pixels together in a region until the emission line in that region achieves sufficient S/N, which we chose here to be 3. This allows us to explore the spatial resolution in areas with high S/N and to examine those regions with low S/N in meaningful spatial regions.

## 4. MAPS AND DATA CUBES

### 4.1. NIRC2 Near-infrared Images

Taken at the  $0''.01$ -per-pixel narrow-camera mode, the  $H$ - and  $K'$ -band NIRC2 images provide an unprece-

dent high-resolution view of the nuclear components in these wavelengths (Fig. 4). All three components, as denoted by the crosses corresponding to the N, SW, and SE, are distinct in both bands.

Exhibiting a disk morphology different from that seen in the optical bands, the N component is both extended and clumpy in the near-infrared. We used GALFIT (Peng et al. 2002, 2010) to quantitatively characterize its morphology and find that the underlying structure is best fit by a central point source (which we call N1) plus a Sérsic profile of index  $n = 1.63$  and effective radius  $r_{\text{eff}} = 0''.69 \pm 0.01$ , or  $520 \pm 8 \text{ pc}$ , in the  $H$ -band continuum. In order to avoid the dusty region between the nuclei, we performed the GALFIT analysis on the eastern half of the disk only (see Fig. 5). The residual map shows some underlying substructure in the disk, but otherwise a Sérsic disk plus central point source model (Fig. 5 top) were a better fit for the N component than one without the central point source (Fig. 5 bottom). In Fig. 4, approximately  $0''.2$  to the northeast of N1 is N2, which looks like a faint, compact clump. It is brighter in the  $K'$  band than it is in the  $H$ ; the difference may be due to dust extinction. It appears distinct and could plausibly be the site of a stellar cluster. It closely coincides with the N2 as designated by Carilli & Taylor (2000), at the location of a hypothesized clump of supernovae. To the southeast of N1 at a distance of  $\sim 0''.15$  is N3, which is extended and elongated in the E-W direction. It may be diffuse emission associated with N1 given its proximity, or it may be a separate clump. There is a larger difference in the brightness of N1 and N3 in the  $K'$ -band relative to that in the  $H$ -band, indicating that N1 is redder than N3.

Lying  $\sim 1''.0$ , or  $750 \text{ pc}$ , to the southwest from N1, the SW component is also resolved at these scales with a north-south extension ( $r_{\text{eff}} = 68 \pm 8 \text{ pc}$  in the  $H$ -band and  $38 \pm 8 \text{ pc}$  in the  $K'$ -band). The high-resolution  $0''.01/\text{pixel}$  data further constrain the size of this compact emission. Detected more notably in the  $H$ -band, the north-south extended feature appears asymmetric and elongated toward the south. The northern extension resembles a tidally-disrupted feature, which suggests that it is material that has not yet settled during the course of the merger. The SW source appears the reddest in the frame, most likely due to dust. This extinction obscures it entirely in the *HST*  $B$ -band image (Fig. 1).

Two distinct sources can be seen in the southeast region relative to the N disk. The southernmost one is compact and appears to be a star cluster. The one denoted with a cross (see Fig. 4) is more diffuse and extended; it marks the site of the SE source seen in radio images (Carilli & Taylor 2000; Bondi et al. 2005). Its spatial extent is larger than the compact source to the south from which the PSF is confirmed. This suggests that the SE component may not simply be a stellar cluster as was suggested by the NICMOS images (Scoville et al. 2000). Given its proximity to the N component and the morphology of the low surface-brightness feature between it and the N component, the SE source may be associated with the N component.

### 4.2. $K$ Broadband Integrated OSIRIS Spectra

In the  $K$  broadband spectra ( $0''.1$ -per-pixel resolution), only two spatially-segregated components appear in the

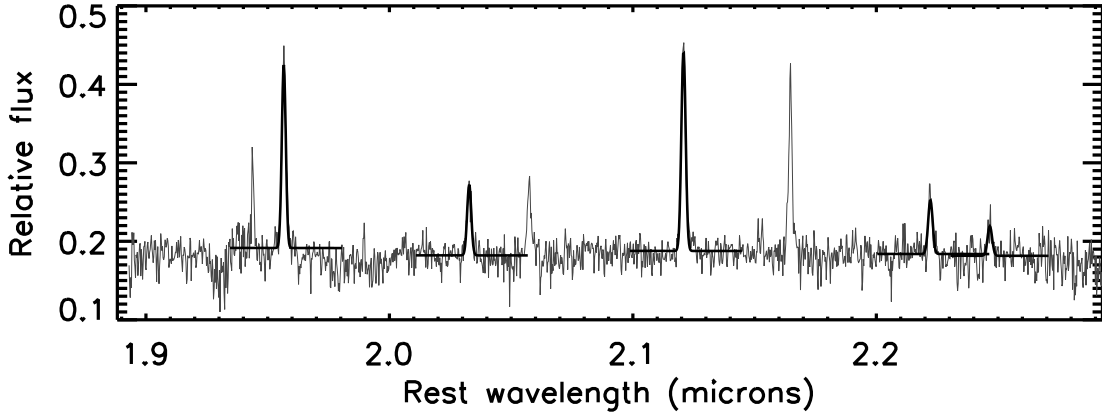


FIG. 2.— Simultaneous fitting of the different  $H_2$  transitions for an arbitrarily-selected pixel as detected in the Kcb data cube. The thin grey line represents the data spectrum; the thick black lines represent the model fits. For each spectrum, all  $H_2$  lines are required to have the same velocity and velocity dispersion; flux is fitted separately for each line. A similar fitting routine is used for  $Br\gamma$  and  $Br\delta$ .

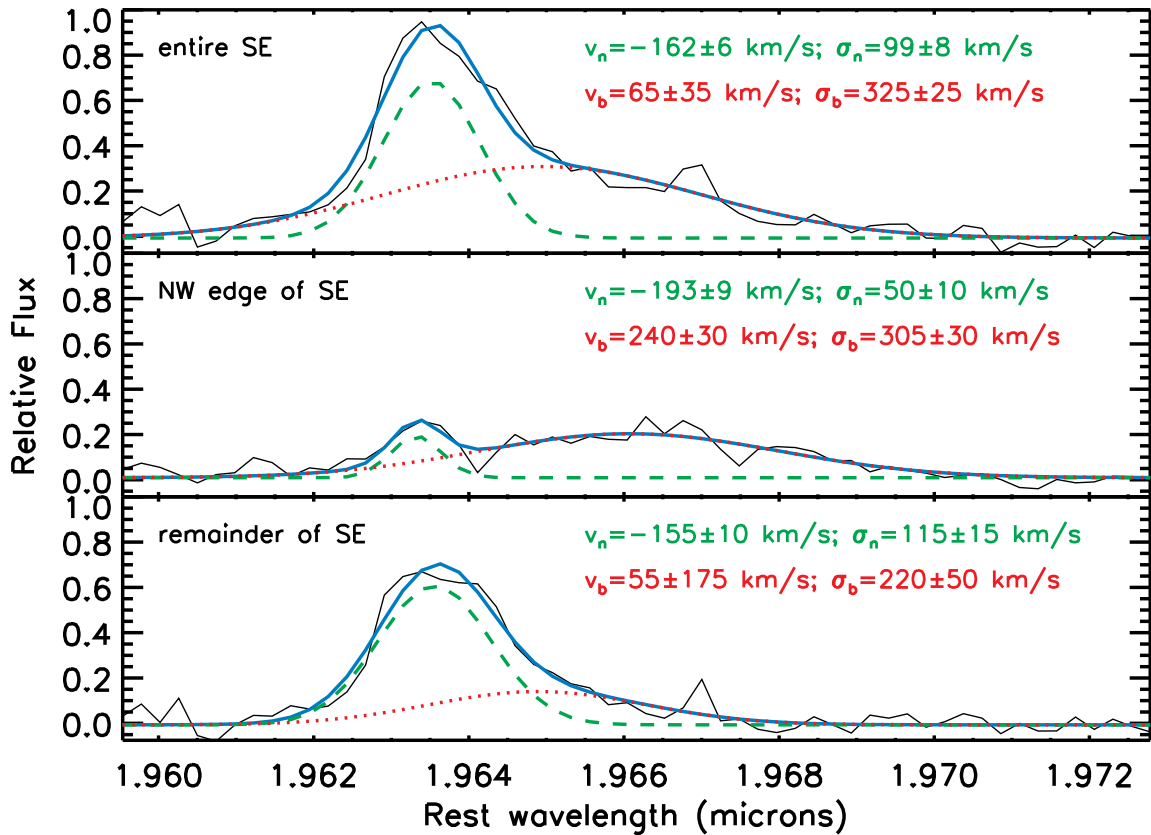


FIG. 3.— A double-Gaussian component-fit to the  $[Si\ vi]$  line profile in three regions of the integrated SE component. The top panel includes the entire SE component; while the middle and bottom panels split the spectrum into the northwest edge and remaining pixels. (These regions are identified in the middle panel of Fig. 10.) In each panel, the black line represents the data spectrum; the green dashed and red dotted lines represent the two components that contribute toward the total model fit in solid blue. In the total spectrum, the  $[Si\ vi]$  line clearly shows two velocity components: one with a narrow velocity dispersion and one with a broader velocity dispersion. We find by splitting the spectrum up spatially that the broader velocity component comes mainly from the northwest edge of the SE component, while the narrow portion of the line appears more heavily in the remaining section. Parameters for each fitted component are listed in each panel.

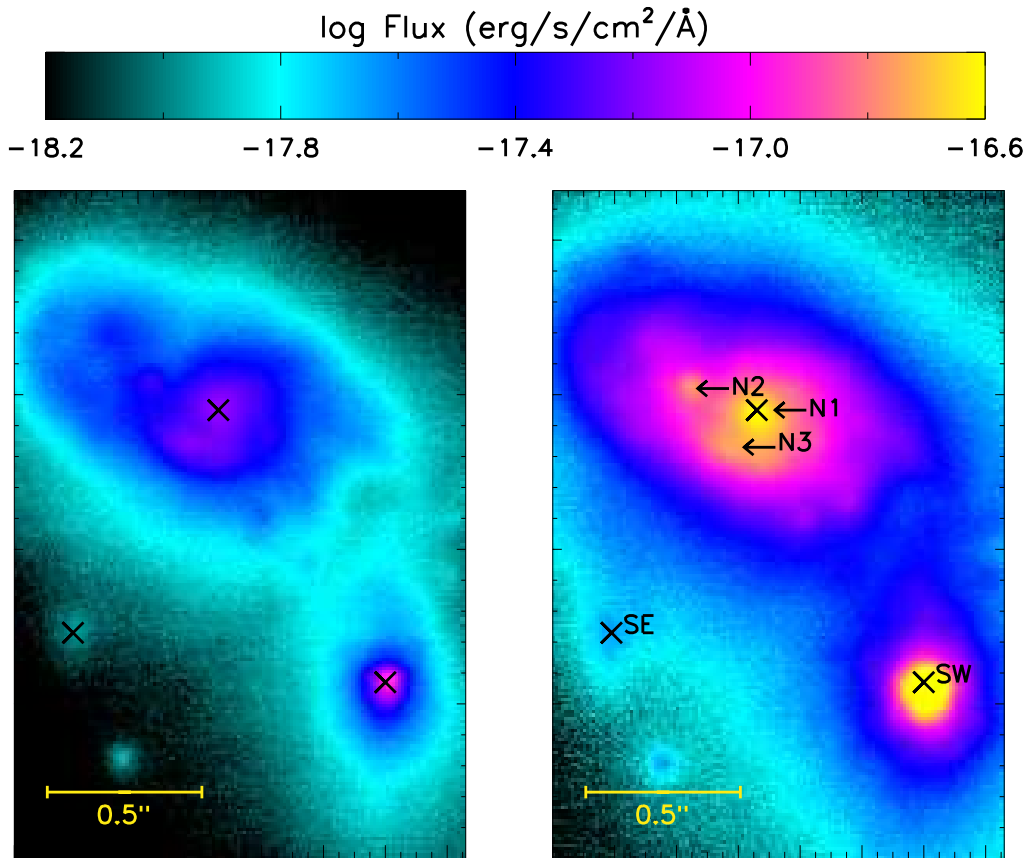


FIG. 4.— Keck NIRC2  $H$ - (left) and  $K'$ -band (right) images taken with the narrow camera ( $0''.01$  pixel scale). The two images are displayed in logarithmic scale in units of  $\text{erg/s/cm}^2/\text{\AA}$  with N pointing up. These images reveal clumpy structure and wispy gas in the nuclear regions of Mrk 273. Crosses denote the three components from Fig. 1, and the arrows point to three different clumps resolved in the N component. See text for a detailed discussion of each.

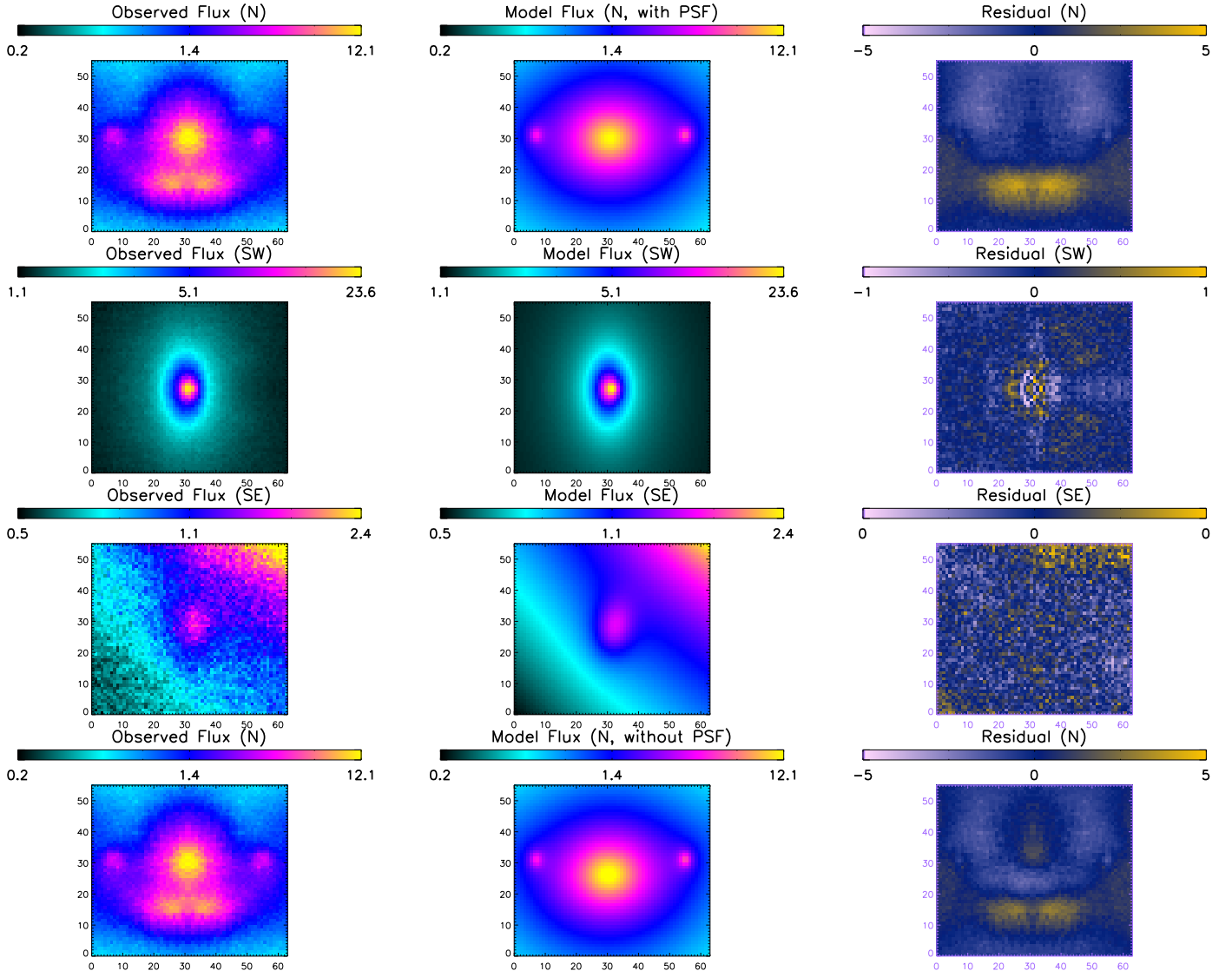


FIG. 5.— Example of fitting results of GALFIT: here, the N (top row), SW (second row), SE (third row), and N (without central PSF in model; bottom row) components in the NIRC2  $H$ -band image have been fitted with a Sérsic, Sérsic, Gaussian, and Sérsic profile, respectively. The leftmost column shows the input data that were fed into GALFIT; the middle column demonstrates the best-fit model parameters; the rightmost column indicates the residual maps. In the case of the N and SW components, we performed GALFIT analysis on a mirrored version of the eastern and southern halves, respectively, in order to avoid the dusty region between the nuclei.

continuum of Kcb: the N extended emission and the SW compact source. The SE diffuse clump is very weak in the integrated image. Fig. 6 shows the integrated spectra of the N, SW, and SE components, respectively. These spectra exhibit very different features. The SW spectrum is dominated by the continuum and has strong [Si VI]  $1.964\ \mu\text{m}$  and  $\text{H}_2$  emission; other emission lines are present but weak. The N spectrum features multiple extremely strong  $\text{H}_2$  transitions along with  $\text{Br}\gamma$  and He I. The SE component is weak in the continuum but exhibits emission in the  $\text{H}_2$ , [Si VI], and Brackett lines as well.

Line parameters of the various regions such as the effective radii for the fitted Sérsic component or FWHM of the fitted Gaussian component, axis ratios, integrated flux ratios, mean velocities, and velocity dispersions are listed in Table 1. The integral-field capability of OSIRIS allows the examination of the spatial distributions and kinematics of these emission lines individually; we present these

results in the following section.

#### 4.2.1. $\text{H}_2$

Five vibrational transitions of molecular hydrogen lie within the Kcb coverage of OSIRIS:  $1-0\ \text{S}(3)$  [ $\lambda_{\text{rest}} = 1.9576\ \mu\text{m}$ ],  $1-0\ \text{S}(2)$  [ $\lambda_{\text{rest}} = 2.0338\ \mu\text{m}$ ],  $1-0\ \text{S}(1)$  [ $\lambda_{\text{rest}} = 2.1218\ \mu\text{m}$ ],  $1-0\ \text{S}(0)$  [ $\lambda_{\text{rest}} = 2.2235\ \mu\text{m}$ ], and  $2-1\ \text{S}(1)$  [ $\lambda_{\text{rest}} = 2.2477\ \mu\text{m}$ ] (hereafter  $\text{H}_{2a}$ ,  $\text{H}_{2b}$ ,  $\text{H}_{2c}$ ,  $\text{H}_{2d}$ , and  $\text{H}_{2e}$ , respectively). These vibrationally-excited emission lines trace the warm molecular gas, and result from a mixture of thermal and nonthermal components, where the excitation mechanisms may involve shock heating, UV photoionization by O and B stars, or X-ray ionization (Mouri 1994). The intensity ratios among these lines can be used to distinguish between the thermal and non-thermal excitation mechanisms due to the difference in their efficiencies in populating the various vibrational levels.

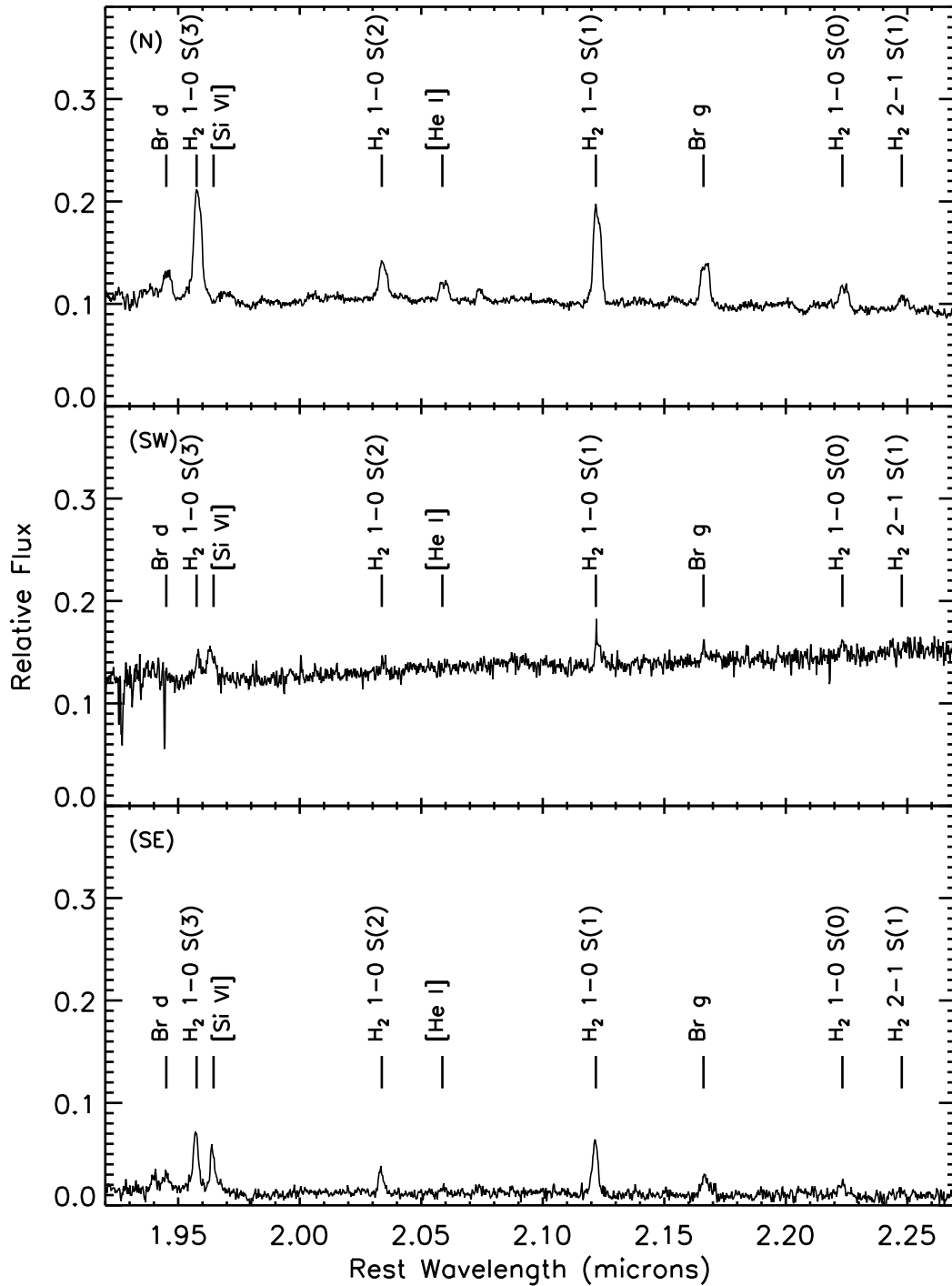


FIG. 6.— OSIRIS integrated spectra of the N component (top), the SW component (middle), and the SE component (bottom) from 50-minutes of on-source exposure, taken in  $K$ -band with the  $0''.1$ /pixel lenslet. Lines of interest are labeled. The telluric-corrected continuum in the SW still shows a steeper gradient than in the N and SE, indicating the presence of hot dust. The SE spectrum shows comparatively little continuum emission but clear evidence of line emission. Most emission lines in the SW are relatively weak. On the other hand, [Si VI] appears strongly in the SW and the SE but not in the N component.

TABLE 1  
PARAMETERS OF THE DIFFERENT REGIONS

Region	Line	$r_{\text{eff}}$ (arcsec)	$r_{\text{eff}}$ (pc)	Axis Ratio	Flux Ratio	$\bar{v}$ (km/s)	$\sigma$ (km/s)
N	H <sub>2c</sub>	0.27±0.01	204±8	0.75±0.01	1.15±0.01	6±2	225±2
	Brγ	0.30±0.06	226±45	0.75±0.01	0.48±0.02	21±7	228±7
	He I	0.27±0.01	204±8	0.75±0.01	0.22±0.02	45±15	230±20
	[Si VI]	..	..	..	..	..	..
	[Fe II]	0.40±0.04	302±30	0.78±0.01	0.13±0.01	6±4	213±9
	H-band continuum	0.69±0.01	520±8	0.74±0.01	..	..	..
	K'-band continuum	0.80±0.01	603±8	0.88±0.01	..	..	..
SW	H <sub>2c</sub>	..	..	..	0.29±0.03	50±15	180±15
	Brγ	..	..	..	..	..	..
	He I	..	..	..	..	..	..
	[Si VI]	0.14±0.02*	106±15	0.08±0.2	0.37±0.06	-290±35	220±50
	[Fe II]	..	..	..	0.04±0.04	7±30	155±45
	H-band continuum	0.09±0.01	68±8	0.41±0.01	..	..	..
	K'-band continuum	0.05±0.01	38±8	0.47±0.01	..	..	..
SE	H <sub>2c</sub>	0.14±0.03*	106±24	0.56±0.05	0.59±0.02	-117±4	173±4
	Brγ	0.07±0.04*	53±30	0.42±0.05	0.30±0.03	45±20	240±20
	He I	..	..	..	..	..	..
	[Si VI]	0.16±0.02*	121±15	0.66±0.09	0.29±0.03	-125±20	150±15
	[Fe II]	0.06±0.01*	45±8	0.23±0.05	0.06±0.04	-10±40	205±60
	H-band continuum	0.06±0.01*	45±8	0.61±0.04	..	..	..
	K'-band continuum	0.13±0.01*	98±8	0.51±0.01	..	..	..
Bridge	H <sub>2c</sub>	0.35±0.03*	264±23	0.68±0.04	0.73±0.02	-125±4	175±5
	Brγ	0.38±0.14*	287±106	0.16±0.06	..	..	..
	He I	..	..	..	..	..	..
	[Si VI]	0.13±0.03*	98±23	0.17±0.06	..	..	..
	[Fe II]	..	..	..	0.10±0.01	-110±15	240±20
	H-band continuum	..	..	..	..	..	..
	K'-band continuum	..	..	..	..	..	..

<sup>a</sup>  $r_{\text{eff}}$  is the effective radius for the fitted Sérsic component; in the \* cases, this is the  $\frac{\text{FWHM}}{2}$  of the fitted Gaussian component.

<sup>b</sup> .. indicates weak or no detection.

Shock-excited  $H_2$  emission has been observed in many galaxies; a notable object among these observations is the prototypical late-stage merger NGC 6240 with dual AGN at  $L_{\text{IR}} = 10^{11.93} L_{\odot}$ , for which the thermal  $H_2$  temperature was determined to be 2000 K (Mouri 1994). Draine & Woods (1990) further proposed that most of the  $H_2$  line emission in NGC 6240 is attributed to X-ray irradiation from either supernova explosions or high-velocity shock waves associated with the merger. Like NGC 6240, Mrk 273 displays prominent emission in  $H_{2c}$ . Fig. 7 shows the unbinned flux, Voronoi-binned velocity and velocity dispersion maps of  $H_{2c}$  along with the distribution of the  $K$  band continuum in contours. The  $H_{2c}$  flux is extended in the N component. In addition, the flux bridges toward the SE component, which is the site of radio continuum emission ( $\sim 1''$  southeast of the N peak).

A velocity gradient typical of an inclined rotating disk can be seen in the velocity map of  $H_{2c}$  (middle panel in Fig. 7). The range of the velocity is  $[-206, 220]$  km  $s^{-1}$ ; the rotational axis of the rotating disk has a PA of  $330^\circ$ . The velocity map spans a larger region beyond the extent of the N disk. Of particular note are the negative velocities extending toward the SE component along the bridge in the emission. Along the major axis of the disk, we measure a velocity dispersion of  $\sim 140$  km  $s^{-1}$ ; along the minor axis and toward the SE, this increases to  $\sim 200$  km  $s^{-1}$  (right panel in Fig. 7). This lends evidence to the presence of biconical collimated turbulent outflows from the center of the N source; the significance of this outflow is further discussed in §5.

#### 4.2.2. Excitation Mechanisms of $H_2$

Multiple  $H_2$  transitions are prominent in the Kcb data, particularly within the N disk. Using equations from Reunanen et al. (2002) and Rodríguez-Ardila et al. (2004, 2005) that make use of the ratios among the various  $H_2$  transitions (e.g.  $H_{2e}/H_{2c}$  and  $H_{2b}/H_{2d}$ ), we can gain insight into the temperature conditions within Mrk 273's nuclei. The rotational temperature does not vary significantly across the nuclear regions. Integrating over the regions defined by the different components, we derive for the N disk a vibrational temperature  $T_{\text{vib}} \simeq 2590 \pm 80$  K and a rotational temperature  $T_{\text{rot}} \simeq 1605 \pm 115$  K. The measured  $T_{\text{vib}}$  is consistent with that measured for a sample of Seyferts ( $T_{\text{vib}} \lesssim 2600$  K) from Reunanen et al. (2002). In addition, the fact that the values for  $T_{\text{vib}}$  and  $T_{\text{rot}}$  differ appreciably suggests that the thermal excitation may be due to fluorescence (Rodríguez-Ardila et al. 2004). The computed  $H_2$  line ratios along with derived temperatures for the various components are listed in Table 2.

$H_2$  gas in galaxies can be excited by a number of mechanisms in the interstellar medium: UV fluorescence, shocks, and X-ray heating (Shull & Beckwith 1982, and others). A diagnostic involving the ratios of different  $H_2$  transitions can be used to distinguish among the various means of exciting the gas (Rodríguez-Ardila et al. 2004). The  $H_{2e}/H_{2c}$  and  $H_{2a}/H_{2c}$  ratios in these nuclear regions are consistent with slow shocks ( $v_s \sim 10 - 14$  km  $s^{-1}$ ) being driven into very dense gas ( $n = 10^5$   $\text{cm}^{-3}$ ; Shull & Hollenbach 1978).

#### 4.2.3. Atomic Hydrogen and Helium

After the various transitions of  $H_2$ , the  $\text{Br}\gamma$  line [ $\lambda_{\text{rest}} = 2.166\mu\text{m}$ ] and the He I line [ $\lambda_{\text{rest}} = 2.059\mu\text{m}$ ] are the next most prominent emission lines in the N spectrum.  $\text{Br}\gamma$  is an indicator of the ionizing radiation field and stellar activity, and has been detected in many Seyfert galaxies (e.g. Riffel et al. 2006). The ionization energy of atomic helium is 24.6 eV; therefore, He I line emission is expected to originate from regions with the most massive and youngest stars (Böker et al. 2008).

Fig. 8 and Fig. 9 show the flux, velocity, and velocity dispersion of the  $\text{Br}\gamma$  and He I lines, respectively. The  $\text{Br}\gamma$  flux, and similarly the He I flux, is detected in the N disk and appears clumpy around the center; this may be due to clumpy star formation in the circumnuclear regions. The depression in flux of these atomic gases at the nucleus may suggest heavy obscuration by dust or ionization of the gas by a strong source like an AGN. The bulk of the  $\text{Br}\gamma$  gas coincides with the N continuum emission. There is very little  $\text{Br}\gamma$  emission at the SW component, but there is  $\text{Br}\gamma$  emission extending toward the SE source, albeit much weaker than in the  $H_2$  lines. There is also faint He I emission in the vicinity of the SE source.

$\text{Br}\gamma$  and He I also display similar kinematics. The velocity structure of a strongly rotating disk similar to that of  $H_2$  is found for  $\text{Br}\gamma$  and He I. The centers of the rotating gas disks coincide with the peak of the continuum flux. The velocity dispersion at the disk is  $\sim 100$  km  $s^{-1}$  but increases to  $\sim 170$  km  $s^{-1}$  at the center. We see no evidence of a broad line region.

#### 4.2.4. [Si VI]

[Si VI] [ $\lambda_{\text{rest}} = 1.964\mu\text{m}$ ], a near-infrared tracer of AGN activity due to its high excitation potential (= 167 eV; Rodríguez-Ardila et al. 2004), has a very different spatial distribution than the other species, as seen in Fig. 10. A fit to the line in the SE region with a Gaussian profile returns poor residuals. A visual inspection prompted us to add a second velocity component which significantly improved the fit (Fig. 3). Two kinematically-segregated components in this region are traced by [Si VI]: a narrow component with velocity  $v_n = -162 \pm 6$  km  $s^{-1}$  and velocity dispersion  $\sigma_n = 99 \pm 8$  km  $s^{-1}$ ; and a broad component with  $v_b = 65 \pm 35$  km  $s^{-1}$  and  $\sigma_b = 325 \pm 25$  km  $s^{-1}$ .

The bulk of the [Si VI] emission is found not in the N disk, likely due to heavy extinction, but at the bridge and the SE component. In the unbinned flux map (Fig. 10), it extends N-S and spans a  $0''.189 \times 0''.163$  (143 pc  $\times$  123 pc) region. Its velocity and velocity dispersion are highest near the bridge, though its relatively low S/N ratio limits the precision with which the location of the emission can be determined. [Si VI] is also strongly detected at the SW component, the site of the hard X-ray AGN (Iwasawa et al. 2011a). The peak position of the [Si VI] flux roughly coincides with that of the continuum, with  $v = -290 \pm 30$  km  $s^{-1}$  and  $\sigma = 222 \pm 50$  km  $s^{-1}$ .

#### 4.3. H Band Integrated Spectra

At a scale of  $0''.035$  per pixel, the Hn4 continuum emission maps the resolved, clumpy N disk and compact SW component. Fig. 11 shows the integrated spectra of the N, SW, and SE components, respectively, highlighting the [Fe II] line found in all three regions. The [Fe II] line

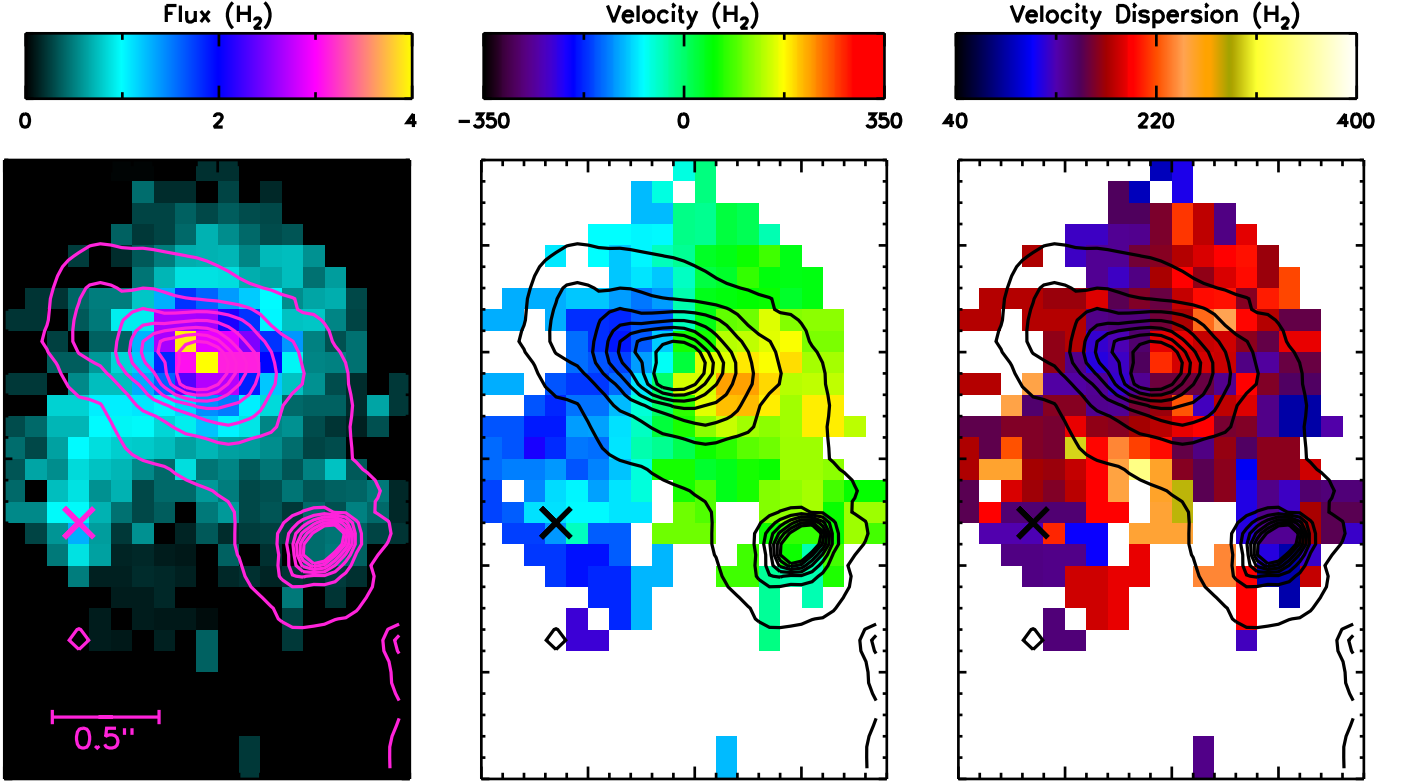


FIG. 7.— (Left to right) The moments 0, 1, and 2 maps corresponding to the unbinned flux, binned velocity, and binned velocity dispersion maps of  $H_{2c}$  in the central region of Mrk 273. Pixels with low signal-to-noise ratio have been removed from the kinematics maps. Contour levels represent the continuum flux, with cross marking the SE region. Bar denotes  $0''.5$ ; N points up. A bridge in flux connects the N and SE components. The bridge shows negative velocities and increased velocity dispersions. The velocity map also reveals strong rotation in the N component; here, velocity dispersion increases in conical regions along the minor axis, possibly revealing biconical collimated outflows from the center of the disk.

TABLE 2  
 $H_2$  LINE RATIOS

Line Ratios	N	SW	SE	Bridge	Total (Mean)	Total (Median)
$H_{2a}/H_{2c}$	$1.19 \pm 0.02$	$0.31 \pm 0.07$	$0.55 \pm 0.03$	$0.75 \pm 0.04$	0.70	0.75
$H_{2b}/H_{2c}$	$0.45 \pm 0.01$	$0.11 \pm 0.05$	$0.27 \pm 0.03$	$0.26 \pm 0.03$	0.27	0.27
$H_{2d}/H_{2c}$	$0.29 \pm 0.01$	$0.15 \pm 0.05$	$0.17 \pm 0.02$	$0.20 \pm 0.03$	0.20	0.20
$H_{2e}/H_{2c}$	$0.18 \pm 0.45$	$0.04 \pm 0.12$	...	...	0.11	0.18
$T_{\text{vib}}$ (K)	$2590 \pm 80$	$2535 \pm 740$	$2240 \pm 230$	$1925 \pm 305$	2325	2535
$T_{\text{rot}}$ (K)	$1605 \pm 115$	$740 \pm 150$	$1645 \pm 355$	$1230 \pm 205$	1305	1605

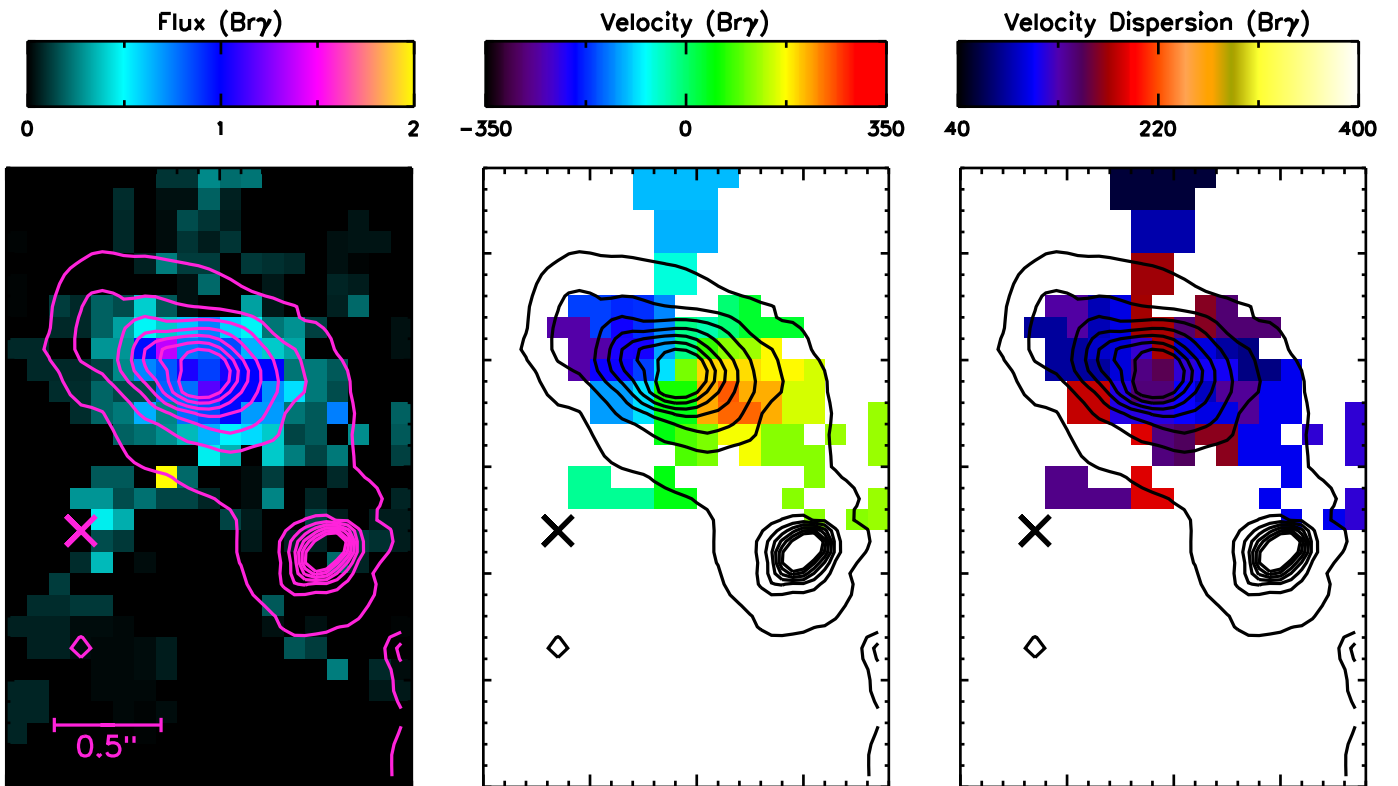


FIG. 8.— Same as Fig. 7, but for Br $\gamma$  (N points up). Br $\gamma$  traces the same rotation in the N component as H $_2$ c, but is much weaker along the bridge to the SE component.

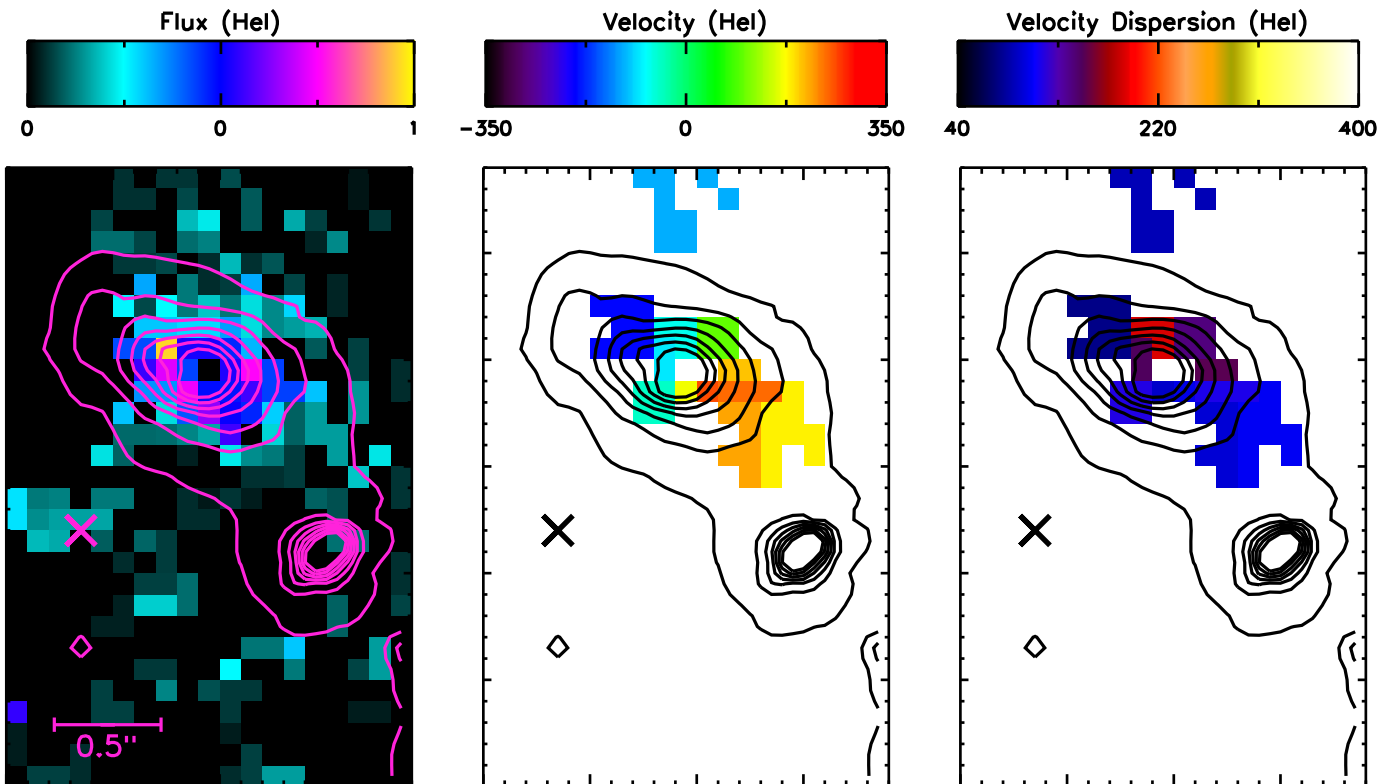


FIG. 9.— Same as Fig. 7, but for He I (N points up). He I traces the same rotation in the N component as  $\text{H}_{2c}$  and  $\text{Br}\gamma$ , but is much weaker along the bridge to the SE component. As with  $\text{Br}\gamma$ , He I flux does not peak at the center of the N component, perhaps due to extinction or a change in the ionizing radiation.

is typically broad ( $\sigma \sim 200 \text{ km s}^{-1}$ ) and prominent in the N and SE components, and dominated by the continuum in the SW. The SE component is weak in the continuum. Line parameters of the regions for the [Fe II] line emission can be found in Table 1.

#### 4.3.1. [Fe II] Emission

In the Hn4 band, the [Fe II] line at  $[\lambda_{\text{rest}} = 1.644 \mu\text{m}]$  shows strong emission in the center of Mrk 273. Because Fe is strongly depleted in the interstellar medium, gas-phase [Fe II] emission (with ionization potential of 16.2 eV; Mouri et al. 1993) in galaxies has been used as a sensitive indicator of shocks (Graham et al. 1987). The potential origins for the [Fe II] emission include regions of partially ionized gas within supernova remnants in starburst nuclei and within narrow-line regions in AGN (Mouri et al. 1993). The contribution from photodissociation regions near O and B stars is negligible. Extracting slices associated with the [Fe II] line from the Hn4 data cube, we present the flux, velocity, and velocity dispersion maps in Fig. 12 with continuum contours for comparison. Like the continuum, the line data

are resolved into multiple clumps in the N disk, but the emission is relatively weak at the N1 site, dominant at N2, and detected at N3. The differences in the line-to-continuum flux ratios between N1 and the other clumps (N1: 0.016, N2: 0.022, N3: 0.022) may suggest that they have different origins (see §5). The [Fe II] line flux is negligible in the SW nucleus but very bright in the SE, with a slightly N-S elongated morphology. The N disk contains more total integrated [Fe II] flux, but the SE peak dominates the surface brightness in the entire inner kpc region. The velocity structure of the [Fe II] line also indicates strong rotation ( $\pm 240 \text{ km s}^{-1}$  centered on the systemic velocity), with high velocity dispersion near the center of the N disk and the strongest velocity dispersion at the SE component.

## 5. DISCUSSION

The mechanisms that power the enormous luminosities in Mrk 273 are likely to be associated with the three nuclear components situated within the dusty core. Here we discuss the nature of these regions.

### 5.1. The Northern Disk

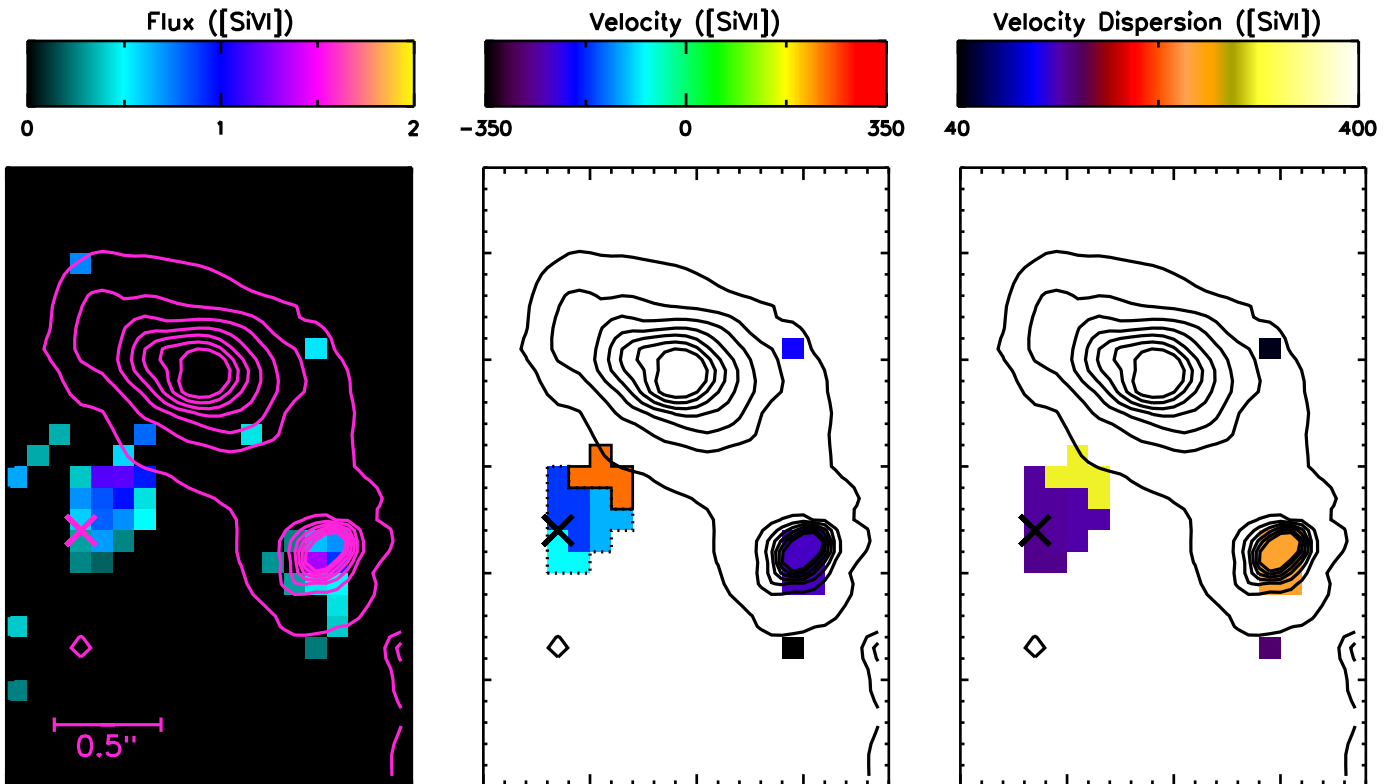


FIG. 10.— Same as Fig. 7, but for [Si VI] (N points up). [Si VI] is undetected in the N component, but appears strongly in the SE and SW components. In the SW, [Si VI] is broad, but see Fig. 3 for a detailed analysis of the SE [Si VI] spectrum, which shows two kinematic components. The two kinematically and spatially segregated regions in Fig. 3 are marked in the center panel: the northwest edge is outlined in solid black, the remaining SE pixels are outlined in dotted black line. The northwest edge shows broader kinematics than the dotted region.

The nature of the N component has been controversial due to different interpretations of the multiwavelength data: clustered radio supernovae (Smith et al. 1998), Seyfert 2 AGN (Xia et al. 2002), and a starburst with the possibility of an additional Compton-thick AGN from excess 6–7 keV emission that might be associated with a high equivalent-width Fe K emission (Iwasawa et al. 2011a). The Fe K line as indicative of a heavily obscured AGN is also present in a dual-AGN LIRG merger Mrk 266, where the LINER nucleus exhibits enhanced shock-excited  $H_2$  emission and diminished coronal line compared to the Seyfert nucleus (Mazzarella et al. 2012). Here, our OSIRIS data cube provides evidence of a strongly rotating gas disk through the distribution and kinematics of the near-infrared emission line gas. The strong  $H_{2c}$  flux suggests localized shocks and fits well with the models of clustered radio supernovae (Smith et al. 1998), lending support to their hypothesis that a starburst provides much of the power. Carilli & Taylor (2000) have resolved individual compact sources that may be supernova remnants; they

suggest that the diffuse emission may be a result of excitation from the remnants. Our OSIRIS data resolve the individual clumps and provide spatial information on the physical conditions of the ionizing source in the N disk. We consider the evidence in this section.

#### 5.1.1. Strong Rotation in Emission Lines

The velocity maps for the emission lines ( $H_2$ ,  $Br\gamma$ , He I, and [Fe II]) detected in the N disk show structure consistent with a strongly rotating disk. The deprojected rotational velocity is  $\sim \pm 240 \text{ km s}^{-1}$ , and its structure is indicative of Keplerian rotation about a large mass (see §5.1.2). We suggest that the rotating disk in the N is the remnant nucleus of a progenitor galaxy in this merger system, with its gas rotating about a central supermassive black hole or a very massive central star cluster. In the next section we use dynamical modeling to determine the enclosed mass.

#### 5.1.2. Black Hole Mass

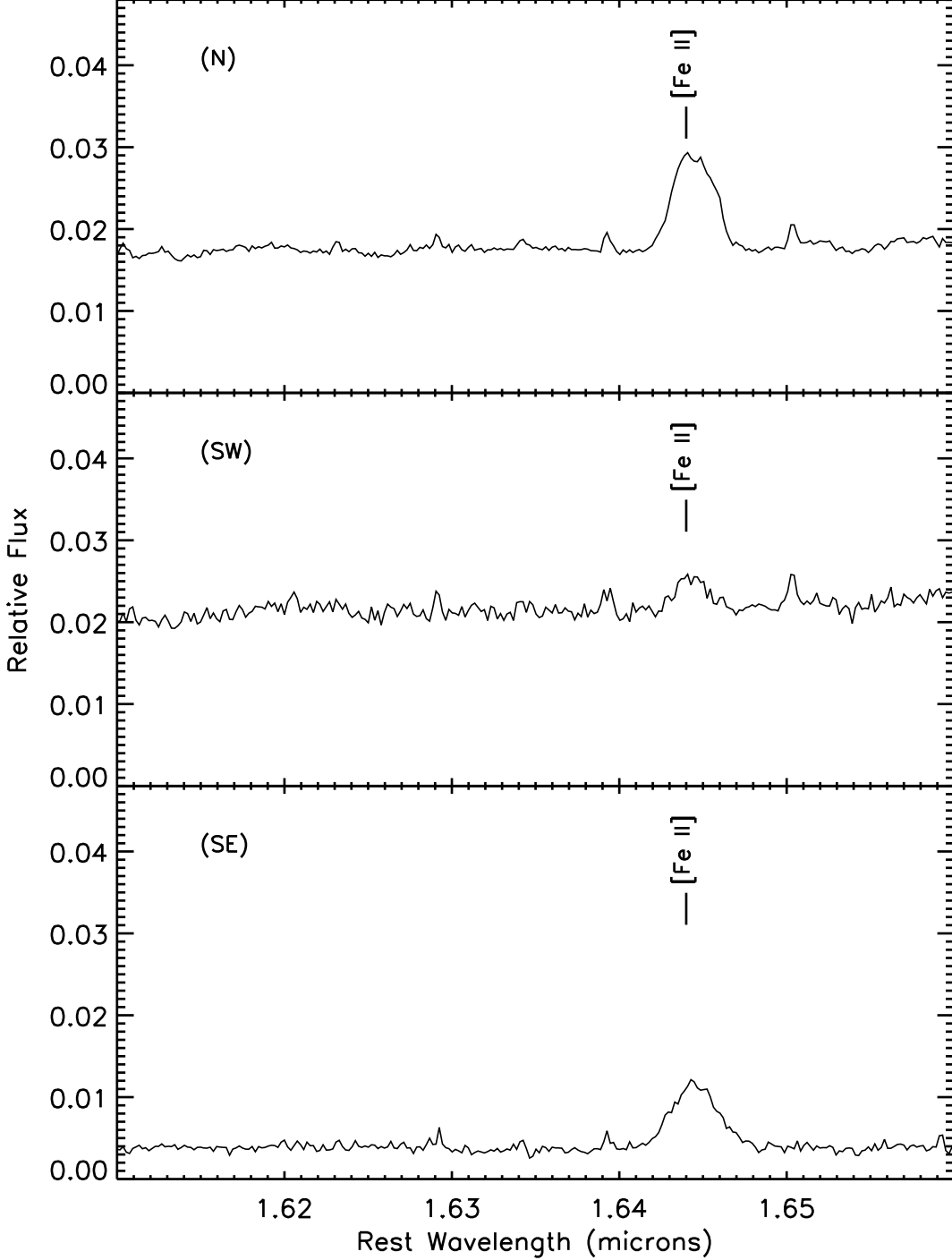


FIG. 11.— OSIRIS integrated spectra of the N (top), SW (middle), and SE components (bottom) from 60-minutes of on-source exposure, taken in  $H$ -band with the  $0''.035$ -scale lenslet. [Fe II] is much stronger in the N and SE components than in the SW component.

From the strong rotation inferred from the emission lines, we measure the kinematics to understand the underlying mass profile. Though rotation in the N disk is seen in every emission line, we focus on the [Fe II] kinematics because these data have significantly higher spatial resolution, by a factor of three, compared to the other emission lines. To measure the dynamical mass of the central source, it is crucial that we resolve within the black hole's sphere of influence. The radius of the sphere

of influence is given by

$$r_{\text{BH}} = \frac{GM_{\text{BH}}}{\sigma^2} \quad , \quad (1)$$

where  $G$  is the Gravitational constant,  $M_{\text{BH}}$  is the mass of the black hole, and  $\sigma$  is the velocity dispersion. We assume a conservative estimate for the mass of the black hole to be  $M_{\text{BH}} \sim 10^9 M_{\odot}$ , given that Klöckner & Baan (2004) had measured a mass of  $1.39 \pm 0.16 \times 10^9 M_{\odot}$  from radio interferometry observations of OH masers. The circumnuclear velocity dispersion we measure from the [Fe II] line is  $\sim 215 \text{ km s}^{-1}$ . Therefore, the radius of

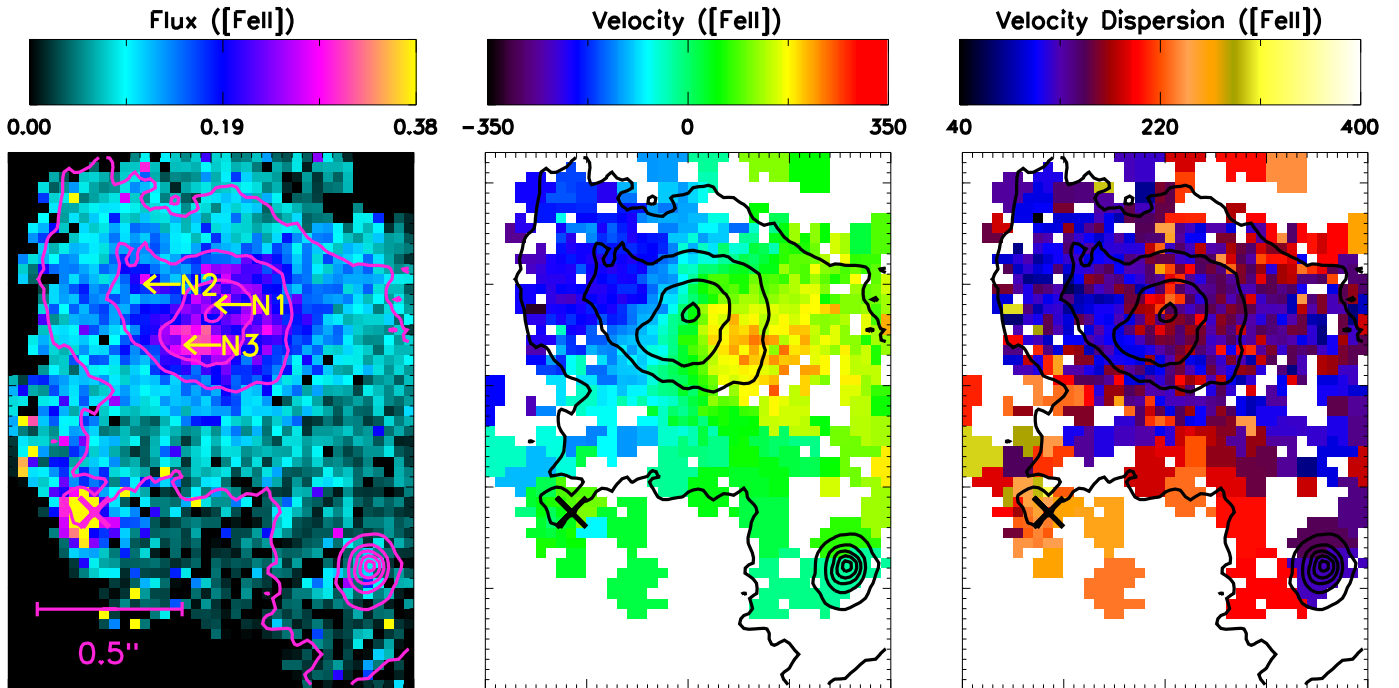


FIG. 12.— Same as Fig. 7 but for [Fe II] ( $\lambda_{\text{rest}} = 1.644\mu\text{m}$ ) from the Hn4 band (N points up). The [Fe II] velocity map shows strong rotation about the N component, with a small increase in velocity dispersion at the center. [Fe II] flux is clumpy in the N component, resolving N1, N2, and N3 due to high resolution as in the NIRC2 images (Fig. 4). However, the fact that N1 is weaker than N2 and N3 could be due to extinction or to differing ionizing radiation fields. The strongest and broadest [Fe II] appears in the SE component.

the sphere of influence is at least  $r_{\text{BH}} \geq 95$  pc. Given our resolution element of  $0''.08$ , or 60 pc, there are 23 spaxels for which the enclosed mass is dominated by the central point mass (see model description below). These spaxels are sufficient to provide a lever arm on black hole mass and, when combined with the surrounding spaxels, enable a reliable dynamical mass measurement from the [Fe II] line kinematics.

We follow the Keplerian disk fitting method outlined in Medling et al. (2011) to compare the measured kinematics to those of simple models. First, we create velocity maps using  $v = \sqrt{GM/r}$  and assuming a central point mass; we also solve for the inclination of the disk and the position of the central point mass. We use the Levenberg-Marquardt least squares fitting routine MPFITFUN (Markwardt 2009; Moré 1978) to select the parameters that best fit the [Fe II] velocity map. We fix the central mass position for generalization to a more complete mass profile. In our second set of models, we estimate the stellar mass profile by fitting a disk to the continuum emission. We subtract off the cen-

tral point-source from the center of the continuum light before fitting. We fit this using the simple radially-varying surface density profile  $\Sigma(r) = \Sigma_0 r^{-\gamma}$ , making the mass in a ring  $2\pi\Sigma_0 r^{1-\gamma} dr$ . We fit the inclination,  $\gamma$ , and  $\Sigma_0$ , and find that the fitted inclination is consistent with the inclination from the first dynamical model ( $55^\circ$ ); we fit a  $\gamma$  of 1.0. In our final set of models we adopt  $v = \sqrt{GM(r)/r}$ , with the mass profile containing a single point mass plus a radially-varying disk mass of surface density  $\Sigma(r) = \Sigma_0 r^{-\gamma}$ . We fix the inclination and the exponent  $\gamma$  from our previous two models, and vary only the point mass and the disk mass density normalization  $\Sigma_0$ . (Note that we allow the last to vary in order to avoid making assumptions about mass-to-light (M/L) ratio. On such small scales, dark matter should be negligible, but estimating a M/L ratio for a stellar population of unknown age with unknown extinctions would introduce more uncertainties than allowing it to be a free parameter.) In each set of models, we convolve our light-weighted model with the PSF (see discussion in §2) before comparing it to our observations. Errors on

parameters have been estimated using a Monte Carlo approach, refitting the black hole mass from a model with 100 iterations of statistical errors and using the resulting distribution.

A comparison between the measured [Fe II] velocity map and the kinematic models is found in Fig. 13. The results illustrate that a disk model with a central point mass turns out a better fit than one without. We find that the best-fit central point mass is  $1.04 \pm 0.1 \times 10^9 M_\odot$ . This mass is consistent with that measured from radio interferometry of an OH maser,  $1.39 \pm 0.16 \times 10^9 M_\odot$  (Klöckner & Baan 2004), and is similar to that of the southern black hole of NGC 6240 ( $8.7 \times 10^8 M_\odot < M_{BH} < 2.0 \times 10^9 M_\odot$ ), another late-stage galaxy merger (see Medling et al. 2011). The mass resemblance to the NGC 6240 black hole suggests that this central point mass may likely be a supermassive black hole. From the kinematics, we cannot determine whether Mrk 273’s N disk hosts a quiescent black hole or a Compton-thick AGN as suggested by Iwasawa et al. (2011a). In either case, the presence of the disk and supermassive black hole confirms that this is the remnant nucleus of one progenitor galaxy.

Though we have shown from our GALFIT analysis that the infrared continuum light profile is best fit with a model of Sérsic disk along with a central point source, we note the possibility that the central mass may be an unresolved massive star cluster instead of a supermassive black hole. Given that massive star clusters found in NGC 6240 have photometric masses of  $7 \times 10^5 - 4 \times 10^7 M_\odot$  (Pollack et al. 2007) and those found in the Milky Way have upper mass limits of  $10^8 M_\odot$  (Murray 2009),  $\geq 10$ -30 of the most massive of these clusters must reside within Keck’s resolution limit to feature the observed kinematics. The two most massive clusters described in Murray (2009) have masses of  $10^8 M_\odot$  and measured radii of  $\sim 100$  pc, suggesting that a cluster 10 times as massive and in a much smaller volume would be improbable. Since it is implausible that  $10^9 M_\odot$  of stars would be dynamically stable within this compact region, we conclude that the central mass must be a supermassive black hole.

### 5.1.3. Spatial Distribution of Line Emission

Br $\gamma$ , which traces ionized gas, and He I, which traces neutral gas, both appear in the N disk. These species both have moderately low velocity dispersion in the disk, and show no sign of being associated with a broad line region. The coronal line [Si VI] is virtually non-existent in the N disk. However, 1.4GHz images from Carilli & Taylor (2000) suggested that there may be a weak AGN present near N1. Similarly, the 6–7 keV extended emission detected near around the N nucleus may be due to enhanced 6.4 keV Fe K line emission, lending support to the presence of a heavily obscured AGN (Iwasawa et al. 2011a). We measure an increase in the velocity dispersion for H $_2$  along the minor axis and toward the SE, which gives direct evidence for the presence of biconical collimated molecular outflows from the N source.

There is a deficiency of Br $\gamma$  and He I flux near N1 compared with the rest of the N disk. This could be due to ionization caused either by an AGN or by supernovae in the center of the disk. However, we find other

putative supernovae sites that do not show a deficiency in Br $\gamma$ , so factors such as extinction may contribute toward this phenomenon near N1. Our Kcb line data are unable to fully resolve the individual clumps in the N disk, but the [Fe II] line and NIRC2 images resolve them at the 0’035 and 0’01 scales, respectively. In particular, N1 is bright in the  $K'$ - and  $H$ -band flux but relatively weak in [Fe II], whereas the faint clump N2 and extended clump N3 have a higher [Fe II]-to-continuum ratio. N3 has similar brightness as N1 in the  $H$ -band, but is weaker than N1 in the  $K'$ -band. The presence and clumpiness of [Fe II] may indicate regions excited by supernova remnants (Alonso-Herrero et al. 1997). However, since N1 is weak in [Fe II] and redder in color than N2 and N3, its ionizing source may be similar to the AGN in the SW component. Given that the supermassive black hole measured dynamically in §5.1.2 lies inside N1, we note the possibility that it may be an obscured AGN.

### 5.2. The Southwestern Nucleus

The SW component is the location of the hard X-ray source from an updated *Chandra* map (Iwasawa et al. 2011a). It is red and unresolved in NICMOS imaging (Scoville et al. 2000), and shows 8.4GHz flux consistent with a radio-quiet AGN (Condon et al. 1991). In our OSIRIS data, this SW region is compact and dominated by the continuum emission. It shows strong [Si VI] and moderate H $_2$  emission, but is weak in Br $\gamma$  flux. At the 0’01 scale of the NIRC2 data, the SW source is resolved and exhibits a N-S extended, asymmetric low surface-brightness structure. The presence of hot dust as inferred from the rising continuum slope agrees with the redness seen at this source in the NICMOS *JHK*-band images (Scoville et al. 2000) as well as with the *Spitzer*-IRS results (Armus et al. 2007), consistent with the presence of an AGN.

The SW nucleus features low detection from H $_2$ , Br $\gamma$ , and He I, all potentially partially destroyed by a strong ionizing source. [Si VI] emission is detected in this region, but is not resolved. It usually indicates the presence of the hard ionizing spectrum of an AGN, consistent with the *Chandra* results that an AGN resides in this source (Iwasawa et al. 2011a).

### 5.3. The Southeastern Component and its Bridge

Though the SE component has been observed in several bands, its nature has remained unclear and controversial. From *HST* ACS and NICMOS images, the SE component resembles a star cluster (Scoville et al. 2000) and is identified as a candidate blue star cluster (CSC1; Iwasawa et al. 2011a). Radio images show prominent emission and extended morphology consistent with AGN jets, but lack the compact core indicative of an AGN. The radio data show a steep spectrum ( $\alpha = 1.4 \pm 0.2$ ), which could point to a starburst origin (Carilli & Taylor 2000; Bondi et al. 2005), though the extended nature ( $\sim 230$  pc) suggests that it is larger than a single star cluster.

Our spectral decomposition of the SE component in the near-infrared adds new information. The SE component appears weak and diffuse in the NIRC2  $H$ - and  $K'$ -band continuum images, but does appear clearly in several emission lines: H $_2$  (Fig. 7), [Si VI] (Fig. 10), and [Fe II] (Fig. 12) in our IFU data. In particular, we note the

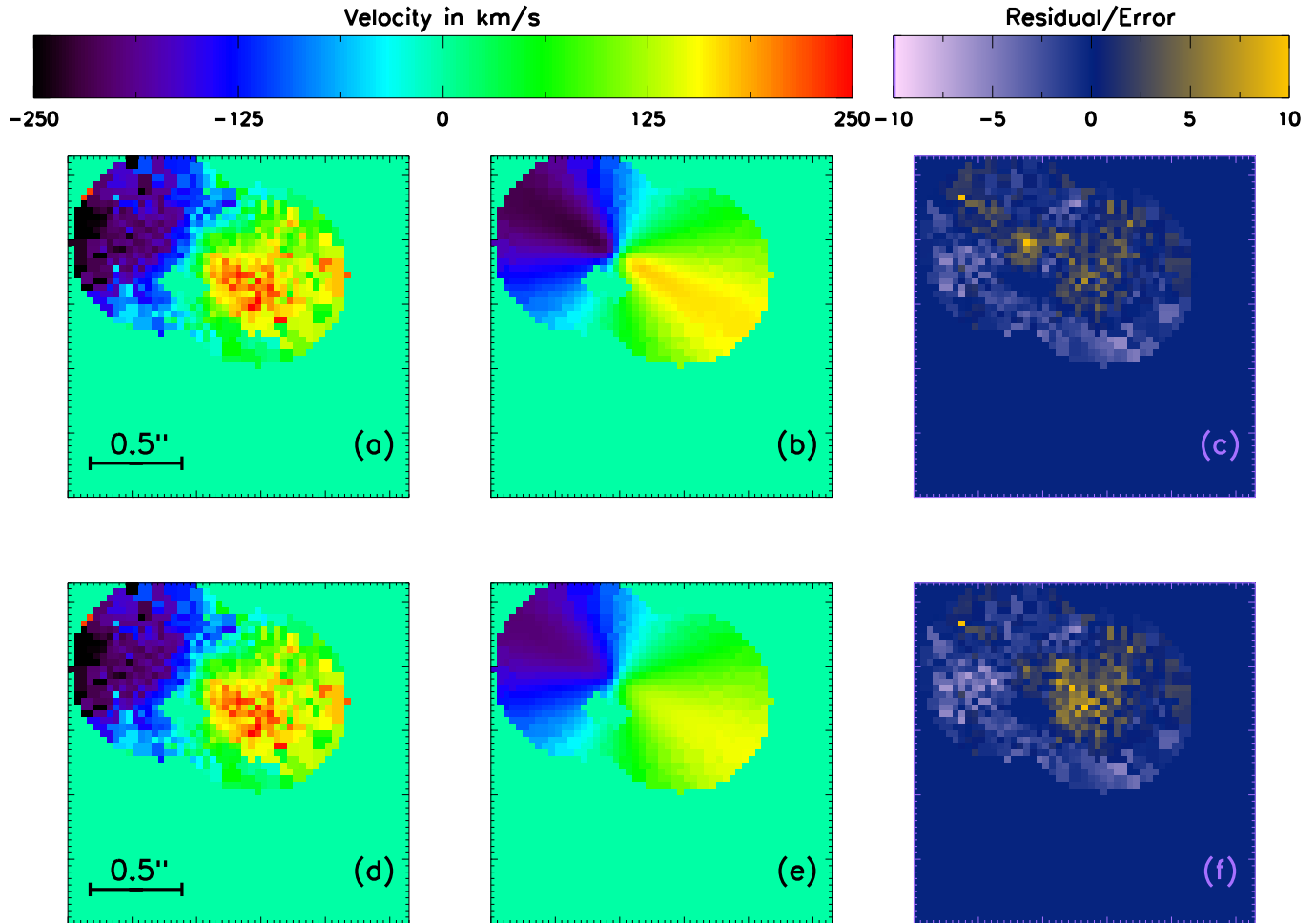


FIG. 13.— These panels show the kinematic modeling comparisons of our measured velocity map of [Fe II] to the velocity map of two rotating disk models with a mass profile containing a radially-varying mass component with (top row) and without (bottom row) a central point mass. (a) data showing [Fe II] velocity map; (b) model with a point mass of  $M = 1.04 \pm 0.1 \times 10^9 M_{\odot}$ ; (c) residuals from data–model as normalized by the error; (d) same as (a); (e) model without central point mass; (f) residuals from data–model without point mass as normalized by the error. All of these panels are masked by a weight map showing only the nuclear region. This comparison shows that the kinematic model incorporating a central point mass is a better fit to the measured velocity map. This suggests the presence of a black hole at the center of the N disk, and that the N is the remnant nucleus of a progenitor galaxy. N points up.

strong [Si VI] emission; as [Si VI] has the highest ionization potential of the observed lines (167 eV), its presence gives a strong clue to the origin of the SE component. The use of [Si VI] as a tracer of the coronal line region (CLR) has been demonstrated by Müller-Sánchez et al. (2011) in 7 nearby Seyfert galaxies. They found that the CLRs in these low-power Seyferts to be  $\sim 80 - 150$  pc in radius and are associated with outflows, providing circumstantial evidence for the existence of extended CLRs and highly ionized gas in outflows from Seyfert nuclei like that in Mrk 273. Here we consider two possible mechanisms to ionize [Si VI]: photoionization and shock-heating. We first consider the [Si VI]/Br $\gamma$  flux ratio in our models; the map of this ratio along with the radial profiles drawn in the direction toward the N and the SW components, respectively, are shown in Fig. 14. We compare the [Si VI] flux to Br $\gamma$  flux since the ratio may give clues to the ionization mechanisms involved. We find that, along the northwest boundary between the SE

component and its bridge, the [Si VI]/Br $\gamma$  ratio reaches 7.9 near the N nucleus, and decreases over  $\sim 0''.3$  to 1.2 near the SE component. We observe a regression slope of  $6.6 \times 10^{-3}$ , which is statistically significant with p-value = 0.03 by permutation. For comparison, we compute the regression slope for a line drawn toward the SW nucleus to be  $-3.9 \times 10^{-4}$ , which is not significantly different from zero. This SE–N line gradient therefore suggests that the north end of the SE component being more highly ionized, and that the origin of the ionization mechanism may be external; we consider below potential sources for the ionization.

### 5.3.1. Photoionized [Si VI]

If the [Si VI] is photoionized, the hard ionizing radiation may come from either an AGN or nearby O and B stars. We compared our measured [Si VI]/Br $\gamma$  flux ratio to those produced by CLOUDY models representing each scenario. We used CLOUDY version 08.00, described

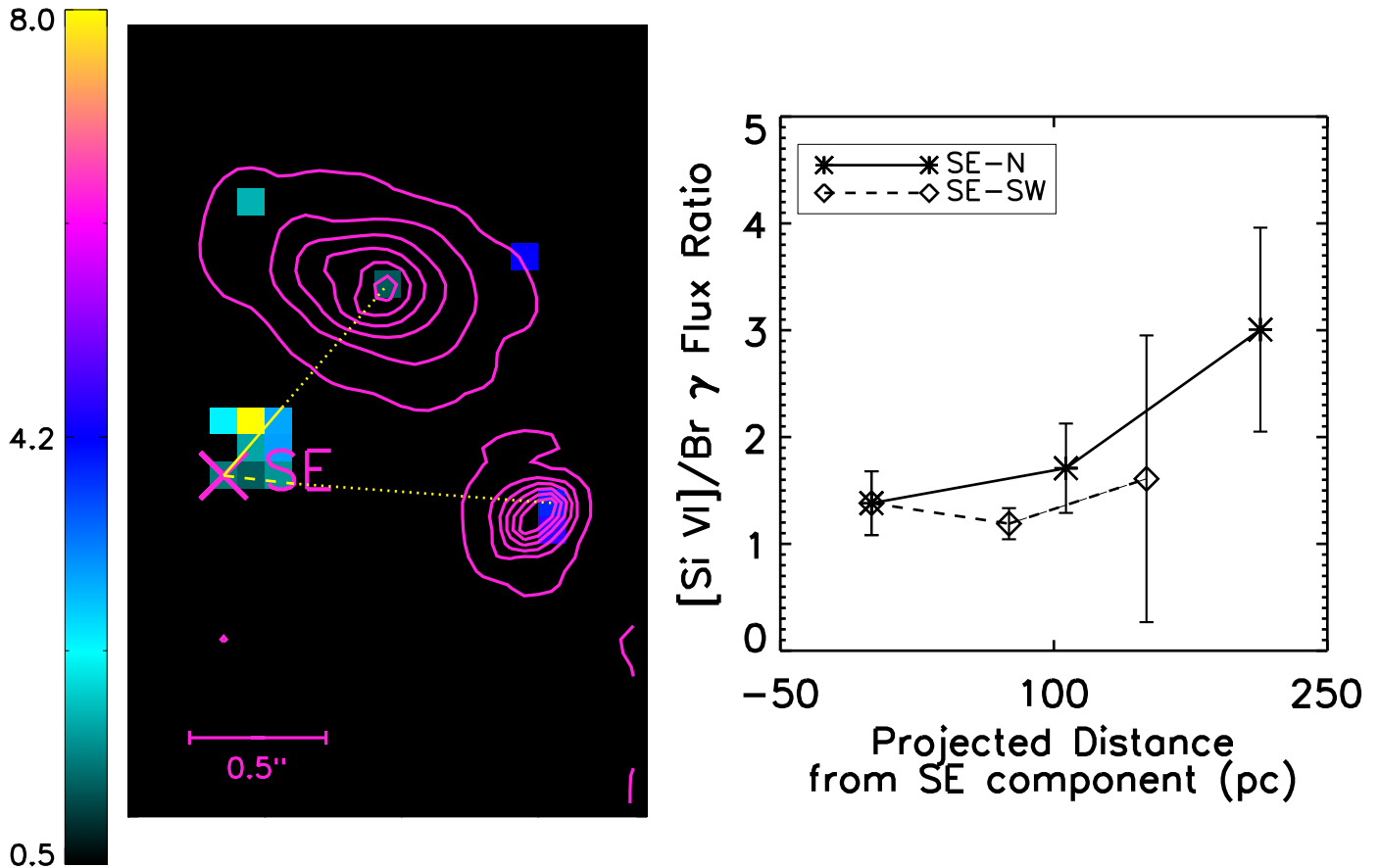


FIG. 14.— (Left) [Si VI]/Br $\gamma$  ratio map with contours showing K band continuum emission. The ratio appears strongest near the northwest boundary between the SE component and its bridge and decreases toward the SE component. This gradient (solid+dotted yellow line) suggests that the origin of the ionization mechanism may be external rather than local. For comparison, a dashed+dotted yellow line is drawn in the direction pointing to the SW nucleus. Bar denotes  $0''.5$ ; N points up. (Right) The radial profile of the [Si VI]/Br $\gamma$  ratio plotted as a function of projected distance from the SE component. The solid and dashed lines correspond to those in the left panel.

by Ferland et al. (1998).

First we confirmed that an AGN can plausibly produce our measured [Si VI]/Br $\gamma$  flux ratio. Our incident AGN spectrum was a power-law continuum with a spectral index of -0.2, and we assumed that the gas is approximately solar metallicity (consistent with estimates from Huo et al. 2004). We varied the ionization parameter of the gas  $U = Q(H^0)/(4\pi r^2 n_H c)$ , where  $Q(H^0)$  is the flux of ionizing photons,  $r$  is the distance between the ionizing source and the illuminated edge of the cloud,  $n_H$  is the volume density of neutral hydrogen to ionize, and  $c$  is the speed of light. We found that, in order to produce a [Si VI]/Br $\gamma$  flux ratio of  $\sim 6$ , an ionization parameter  $U$  of at least  $10^{-2.7}$  is required. When varying the metallicity  $\log(Z/Z_\odot)$  from -0.5 to 1.0, we found that the required ionization parameter varies by less than 0.3 dex. We used  $n_H \sim 10^3 \text{ cm}^{-3}$  as a conservative estimate of the density in the central regions of ULIRGs (but see Davies et al. 2003, whose models suggest the densities can be as high as  $10^4 - 10^5 \text{ cm}^{-3}$ ). We found that the required  $Q(H^0) \sim 4 \times 10^{54} (\frac{r}{750 \text{ pc}})^2 \text{ s}^{-1}$ . A typical

$Q(H^0)$  for a quasar can reach nearly  $10^{57} \text{ s}^{-1}$  (Tadhunter 1996); lower levels of AGN activity would naturally produce fewer ionizing photons. These numbers suggest that photoionization from an AGN in the N disk could plausibly produce our measured [Si VI]/Br $\gamma$  flux ratios, even at a distance of 750 pc. We note that both the N and the SW components, at distances of 640 and 750 pc respectively, fall within this range. However, the spatial distribution of the [Si VI]/Br $\gamma$  flux ratio (see Fig. 14, where the gradient seems to be higher toward the N nucleus) is more consistent with photoionization from a N AGN than from the SW unless there is variable dust extinction surrounding the SE component that alters the angle of the gradient.

We must determine if our measured [Si VI]/Br $\gamma$  flux ratios could instead be produced by nearby O and B stars due to intense star formation. To test this scenario, we used an incident O star spectrum from the Tlusty models described in Lanz & Hubeny (2003). As an extreme case, we chose two of the hottest O star spectra available, with effective temperatures of 55,000K and

52,500K, at solar metallicity and with  $\log(g)$  of 4.5 and 4.25, respectively. Again we varied the ionization parameter  $U$  and the metallicity of the gas to found the required  $Q(H^0)$  to produce our measured  $[\text{Si VI}]/\text{Br}\gamma$  flux ratios. In this scenario, we find that an ionization parameter  $U$  of at least  $\sim 10^{12}$  is required for our measured  $[\text{Si VI}]/\text{Br}\gamma$  flux ratio. This  $U$  value is much higher than is required for an AGN because the AGN spectrum is much harder than that of an O star. To produce this high of an ionization parameter from stars present within 5 pc requires  $Q(H^0) \sim 8 \times 10^{64} (\frac{r}{5\text{pc}})^2 s^{-1}$ . A single O star's  $Q(H^0) \sim 10^{50} s^{-1}$  (see models by Sternberg et al. 2003); for this line ratio to be produced by photoionization from stars, we would need  $10^{14}$  O stars within 5 pc – a completely unphysical scenario. We conclude that if our measured  $[\text{Si VI}]/\text{Br}\gamma$  flux ratios are caused by photoionization, they must be from an AGN.

### 5.3.2. Shock-Heated $[\text{Si VI}]$

$[\text{Si VI}]$  may be ionized in gas heated by shocks and is sometimes observed in novae and supernova remnants (Gerardy & Fesen 2001). Several pieces of evidence in our observations suggest the possibility of outflows that could be causing shocks near the SE component. The  $\text{H}_2$  and  $[\text{Fe II}]$  emission bridge, the increase in  $\text{H}_2$  velocity dispersion along the minor axis, as well as the noted  $[\text{Si VI}]/\text{Br}\gamma$  gradient decreasing along the bridge from the N to the SE component, would be explained by outflows associated with the central powering source within the N nucleus in this scenario – AGN jets or stellar winds. Although the  $[\text{Si VI}]$  emission appears diffuse, the  $\text{H}_2$  velocity map in this region shows a clear shift from the systemic velocity of the system with  $\Delta v \sim -150 \text{ km s}^{-1}$  along the bridge and  $\Delta v \sim -75 \text{ km s}^{-1}$  at the SE component. The spectrum of the H I 21 cm absorption shows a double-peaked profile suggesting infall at  $200 \text{ km s}^{-1}$  on scales  $\leq 40 \text{ pc}$  (Carilli & Taylor 2000). With this evidence of gas motion, it is likely that shocks may exist; these shocks could be responsible for some or all of the measured  $[\text{Si VI}]/\text{Br}\gamma$  flux ratio ( $\leq 7.9 \pm 3.4$ ).

To determine if our observed  $[\text{Si VI}]/\text{Br}\gamma$  flux ratio may be plausibly caused by shocks, we compared it to the shock models of Allen et al. (2008) using the IDL SHOCKPLOT widget. In particular, we adopted the radiative shock plus photoionized precursor model with solar abundance and density  $n = 10^3 \text{ cm}^{-3}$  as a conservative estimate for a ULIRG, and calculated line ratios produced for models within a grid of parameter space. The parameter space in magnetic parameters  $B/n^{1/2}$  and shock velocities  $v_s$  of the model grid is  $B/n^{1/2} = 10^{-4} - 10 \mu\text{G cm}^{3/2}$  and  $v_s = 200 - 1000 \text{ km s}^{-1}$ . The model grid is shown in Fig. 15, with a green symbol marking the value of the line ratios observed in the SE component; it does not appear to converge on any shock model generated within our parameter space. The more robust  $[\text{Si VI}]/\text{Br}\gamma$  ratio (which is less sensitive to dust or cross-filter photometric calibrations) is only produced by models with a high  $B/n^{1/2}$  value and a shock velocity to  $v_s \geq 550 \text{ km s}^{-1}$ , indicating that only fast shocks in the densest material, if at all, could produce the line ratios that are observed in the SE component.

### 5.3.3. Energy Flow from N1

The  $[\text{Si VI}]/\text{Br}\gamma$  ratio, seen as a gradient from the N and decreasing toward the SE, in combination with the bridge between SE and N seen in the other flux maps, strongly suggest an external origin for the source of the observed energy flow, possibly from the center of the N disk. We find that the SE component is likely to be gas from a tidal feature or stellar cluster that is being affected in one of two ways. The easiest way to ionize the  $[\text{Si VI}]$  is with a buried AGN in the N disk or the SW AGN with variable extinction. The AGN would not be isotropically obscured, and thus could photoionize gas in certain directions. However, we find that the observed  $[\text{Si VI}]/\text{Br}\gamma$  ratios may also be produced in extreme shock situations. Here we investigate if such shocks are consistent with our kinematic data, and whether star formation is able to provide sufficient energy to power them.

The spectral maps and kinematics in the region of the bridge suggest its origin as an outflow originating at the center of the N disk. It extends along the minor axis of the disk, following the region of increased velocity dispersion in molecular hydrogen, suggesting that a biconical turbulent outflow is present. The increased  $\text{H}_2$  emission toward the SE has a peculiar velocity of  $-200 \text{ km s}^{-1}$  relative to the systemic velocity of the system; this gas appears to be outflowing. We used simple energy arguments to estimate the amount of energy input required, to determine whether it is likely driven by stellar winds or from AGN feedback. The energy contained in the outflow is  $1/2 mv^2$ , where  $m$  is the mass contained in the outflow and  $v$  is the peculiar velocity,  $-200 \text{ km s}^{-1}$ . To estimate the mass contained in the outflow, we adopted solar metallicity and a density of  $1000 \text{ cm}^{-3}$  (a conservative estimate for (U)LIRGs, see Davies et al. 2003), and used the size of the extended emission (see Table 1) assuming an equal depth and width, resulting in a mass of  $7700 M_\odot$ . To determine an energy input rate, we estimated the amount of time the outflow has been traveling from the distance between the SE and the center of the N disk. To travel this distance of 640 pc at  $200 \text{ km s}^{-1}$ , the outflow requires  $\sim 3.3$  million years. Assuming the energy contained in the outflow was spread out over this timescale, the energy input rate required to drive this outflow is  $1.3 \times 10^{43} \text{ erg s}^{-1}$ .

Is there enough star formation to provide this energy input in stellar winds? We estimate the available energy input from stellar winds as follows: the luminosity of  $\text{Br}\gamma$  in the N disk is  $2.1 \times 10^{40} \text{ erg s}^{-1}$ , implying a star formation rate of  $17 M_\odot \text{ yr}^{-1}$  (Kennicutt 1998) and therefore a bolometric luminosity of  $1.7 \times 10^{11} L_\odot$  (Krumholz & Tan 2007). Approximately 1% of the bolometric luminosity of a starburst is available to drive stellar winds (Heckman 1994), divided by 2 to account for the collimated biconical outflow, yielding an energy input rate available from the N disk's star formation of approximately  $3 \times 10^{42} \text{ erg s}^{-1}$ . However, we note that the computed star formation rate may be underestimated since  $\text{Br}\gamma$  in the N disk may be subject to dust extinction. There may also exist an uncertainty of a factor of a few in the luminosity of starburst-driven winds. Thus, although the energy from star formation seems insufficient by a factor of 4 compared to the required energy input rate, starbursts cannot be definitively ruled out as a source of driving the winds.

It is also important to consider whether the energy

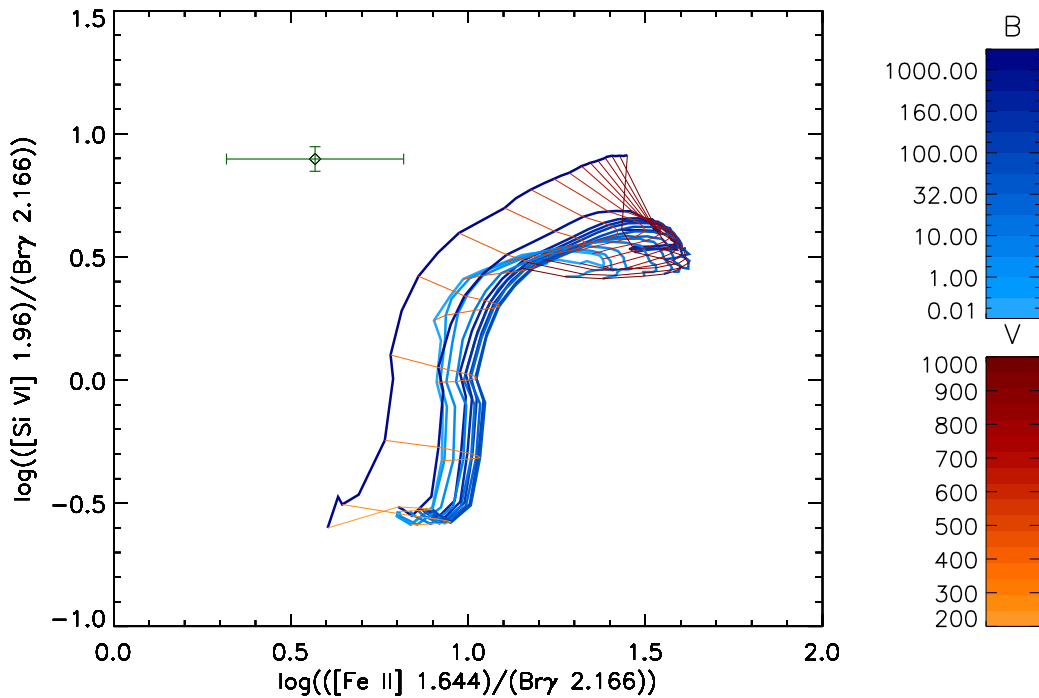


FIG. 15.— Diagnostic plot of  $[\text{Fe II}]/\text{Br}\gamma$  vs.  $[\text{Si VI}]/\text{Br}\gamma$  showing a grid of shock models with solar abundance and density  $n = 10^3 \text{ cm}^{-3}$  (Allen et al. 2008). The parameter space spans magnetic parameters  $B/n^{1/2} = 10^{-4} - 10 \mu\text{G cm}^{3/2}$  and shock velocities  $v_s = 200 - 1000 \text{ km s}^{-1}$ . The green symbol marks the value of the line ratios associated with the SE component; it does not appear to converge on any shock model generated within our parameter space. The more robust  $[\text{Si VI}]/\text{Br}\gamma$  ratio (which is less sensitive to dust or cross-filter photometric calibrations) is only produced by models with a high  $B/n^{1/2}$  value and high shock velocity, suggesting that only fast shocks in the densest material, if at all, could be responsible for its excitation.

available to drive outflows from star formation is sufficient to shock-heat the  $[\text{Si VI}]$  seen in the SE component. The incoming kinetic energy rate is  $e_k = 1/2 \rho v_s^3 A$ , where  $\rho$  is the density (as above,  $1000 \text{ cm}^{-3}$ ),  $v_s$  is the shock velocity ( $\geq 550 \text{ km s}^{-1}$ , calculated from the SHOCKPLOT models in §5.3.2), and  $A$  is the surface area of the gas being shocked. A lower limit on the shocked area is a hemisphere on the surface of the SE component:  $2\pi (70 \text{ pc})^2$ . (In reality, the shock front would likely have structure and therefore larger surface area; this provides a conservative lower limit on the energy input required to shock this  $[\text{Si VI}]$ .) These estimates require an energy input of  $1.7 \times 10^{44} \text{ ergs}^{-1}$ , two and a half orders of magnitude larger than  $5 \times 10^{41} \text{ erg s}^{-1}$ , the available energy for outflows from star formation in the N disk. This suggests that the observed  $[\text{Si VI}]$  emission cannot be caused solely by shock-heating due to stellar winds. Stronger shocks may be plausible with AGN-driven outflows, but because shock models cannot produce the observed  $[\text{Si VI}]/\text{Br}\gamma$  ratio, at least some of the  $[\text{Si VI}]$  emission must be caused by AGN photoionization (as discussed in §5.3.1).

Though photoionization from an AGN is the simplest way to produce the  $[\text{Si VI}]$  emission in the SE, it is likely produced by a combination of the two processes: e.g., a weaker AGN to photoionize some gas, and less extreme shocks to heat the rest. Our observed double-peaked  $[\text{Si VI}]$  velocity profile indicates that there are likely two kinematic components in this region — with broad and narrow velocity dispersions, respectively. The broad component contributes roughly half the  $[\text{Si VI}]$  flux, result-

ing in a  $[\text{Si VI}]/\text{Br}\gamma$  ratio of  $3.9 \pm 1.7$ , or  $0.59^{+0.16}_{-0.25}$  dex in logarithmic units. This constrains the shock models to velocities  $v_s \sim 350 - 450 \text{ km s}^{-1}$ , within the range of the velocity dispersion of the broad component. The two narrow and broad components may have originated from two different heating mechanisms, lending support to the combined AGN and shocks scenario. A simple explanation might involve a combination of shocks from the outflow and photoionization by a buried AGN within the N disk.

The SW AGN is also a potential origin for the photoionizing flux, even though it is further in projection from the SE component. In this alternative scenario, the observed spatial gradient in the  $[\text{Si VI}]$  excitation toward the N nucleus could be caused by differential extinction in the dust between the SW and the SE components, by differential gas densities within the SE component, or by geometric projection effect. Current observations are unable to distinguish between these proposed scenarios, and thus further investigations will be needed to confirm the nature of the ionizing source within Mrk 273's nucleus.

## 6. SUMMARY

High spatial resolution imaging and integral field spectroscopy with Keck laser guide star adaptive optics has allowed us to study the properties of the atomic and molecular emission lines of Mrk 273 in the  $H$ - and  $K'$ -bands. The nuclear region is resolved into three primary components (N, SW, and SE) with a gas bridge between the N and SE components. These near-infrared high-resolution maps are well suited for investigating the gas

dynamics and the location of the hardest photons from AGN and fast shocks; they complement other multiwavelength data for determining the ultimate power associated with each component.

We have shown that the N component is a rotating gaseous disk with PA  $\sim 330^\circ$ . The characteristic size of the disk varies depending on the emission line studied, but the effective radius is roughly  $0''.30$  (240 pc). Using the observed strong rotation, we measure from the kinematics of [Fe II] a central mass of  $M = 1.04 \pm 0.1 \times 10^9 M_\odot$ , consistent with the mass measurement from OH maser kinematics (Klöckner & Baan 2004). This enclosed mass likely indicates the presence of a supermassive black hole at the center of the N disk, suggesting that the N component is the remnant nucleus of a progenitor galaxy. The gaseous disk may be a remnant from the progenitor galaxy or may be recently formed with new gas from the merger. The black hole is heavily obscured and may be an AGN and/or surrounded by additional star formation, consistent with conclusions from X-ray (Iwasawa et al. 2011a) and radio data (Carilli & Taylor 2000; Bondi et al. 2005). An increase in the velocity dispersion of H<sub>2</sub> along the minor axis of the N disk and toward the SE suggests the presence of bipolar molecular outflow originating from the N source. Extended emission of shocked H<sub>2</sub> toward the SE also reveals the presence of a collimated outflow. Energy arguments associated with the size and kinematics of this outflow suggest that it is too massive to be produced by star formation alone, and also point toward the scenario in which the N black hole is a buried AGN. H<sub>2</sub> line ratios offer insight into the rotational and temperature conditions as well as their excitation mechanisms. We derived  $T_{\text{vib}} \simeq 2591 \pm 79\text{K}$  and  $T_{\text{rot}} \simeq 1604 \pm 113\text{K}$ , which fall within the range of temperatures for Seyfert galaxies (Reunanen et al. 2002).

The SW component is bright and compact in the  $K'$ - and  $H$ -band continua, and shows emission of the coronal line [Si VI]. We suggest that a non-thermal photon source is ionizing the silicon and producing the [Si VI] emission that we observe; it would also heat the hot dust that we observe in the continuum. Our near-infrared data support the notion that the SW nucleus hosts the known hard X-ray AGN in this system (Iwasawa et al. 2011a).

The SE component presents a new piece in the puzzle of the merger's nuclear region. While it has previously been detected in the radio regime (Smith et al. 1998), it has not been detected in optical and near-infrared images until now due to the dominance of the broadband continuum. With our new AO-assisted NIRC2 images and OSIRIS integral field spectroscopy, the SE component is detected in several emission lines, and is prominent in both [Fe II] and [Si VI]. The double-Gaussian fit to this [Si VI] line indicates that there are two velocity components involved, perhaps due to outflows. We discussed several potential scenarios for the origin of the SE component: photoionization by AGN or O and B stars, shock-heating due to stellar winds or AGN-driven outflows, or a combination of both. We favor the case where the SE component is a clump of gas or tidal fea-

ture photoionized by an obscured AGN in the N disk and/or shock-heated by outflows from the same AGN and its surrounding star formation. Alternatively, the photoionizing flux affecting the SE component may originate from the SW AGN. Confirming the N black hole as a buried AGN and the nature of the source for the SE component's ionizing radiation will require further investigations. While AGN photoionization alone could produce the observed [Si VI]/Br $\gamma$  ratio, only the most extreme shocks in the shock-heated scenario could account for these [Si VI]/Br $\gamma$  values. We suggest that a combination of photoionization and shocks could best produce both the observed line ratios and the two kinematic components of [Si VI].

As a late-stage gas-rich merger, Mrk 273 offers a unique time in the merger sequence where the nuclei have not completely merged and yet one AGN has already been triggered. We have identified a second black hole, located in the center of the N disk, which may be an obscured AGN with supporting evidence of outflows. The gas disk is likely the remnant nuclear disk from one of the progenitor galaxies, or perhaps a young disk formed during the merger. An understanding of the unveiling of this second black hole as an unburied AGN may lead to a deeper understanding of the frequency of dual AGNs in merging gas-rich galaxies.

We thank the anonymous referee for a helpful discussion on alternative cases for photoionizing the SE component, and for various suggestions on strengthening the scenarios put forth in the paper. We acknowledge H. Inami and S. Stierwalt for providing their *Spitzer*-IRS spectra toward ease of target selection for our observing program; M. Ammons for help with data reduction and PSF estimation; R. da Silva for help with CLOUDY and shock-plot modeling; and D. Rupke for helpful conversations toward the results and their interpretations. We also thank the Keck staff for help with carrying out the observations and the UH/UC TACs for granting this observing time. The data presented herein were obtained at the W.M. Keck Observatory, which is operated as a scientific partnership among the California Institute of Technology, the University of California and the National Aeronautics and Space Administration. The Observatory was made possible by the generous financial support of the W.M. Keck Foundation. The authors wish to recognize and acknowledge the very significant cultural role and reverence that the summit of Mauna Kea has always had within the indigenous Hawaiian community. We are most fortunate to have the opportunity to conduct observations from this mountain. VU acknowledges funding support from the NASA Harriet G. Jenkins Predoctoral Fellowship Project and the Smithsonian Astrophysical Observatory Predoctoral Fellowship. AM acknowledges funding support from the NSF Graduate Fellowship. KI thanks support from Spanish Ministerio de Ciencia e Innovación (MICINN) through grant (AYA2010-21782-C03-01). This work is partially supported by the JPL Contract/IRAC GTO Grant # 1256790.

## REFERENCES

Allen, M. G., Groves, B. A., Dopita, M. A., Sutherland, R. S., & Kewley, L. J. 2008, *ApJS*, 178, 20

Alonso-Herrero, A., Rieke, M. J., Rieke, G. H., & Ruiz, M. 1997, *ApJ*, 482, 747

- Armus, L., Charmandaris, V., Bernard-Salas, J., Spoon, H. W. W., Marshall, J. A., Higdon, S. J. U., Desai, V., Teplitz, H. I., Hao, L., Devost, D., Brandl, B. R., Wu, Y., Sloan, G. C., Soifer, B. T., Houck, J. R., & Herter, T. L. 2007, *ApJ*, 656, 148
- Armus, L., Mazzarella, J. M., Evans, A. S., Surace, J. A., Sanders, D. B., Iwasawa, K., Frayer, D. T., Howell, J. H., Chan, B., Petric, A., Vavilkin, T., Kim, D. C., Haan, S., Inami, H., Murphy, E. J., Appleton, P. N., Barnes, J. E., Bothun, G., Bridge, C. R., Charmandaris, V., Jensen, J. B., Kewley, L. J., Lord, S., Madore, B. F., Marshall, J. A., Melbourne, J. E., Rich, J., Satyapal, S., Schulz, B., Spoon, H. W. W., Sturm, E., U, V., Veilleux, S., & Xu, K. 2009, *PASP*, 121, 559
- Ballo, L., Braitto, V., Della Ceca, R., Maraschi, L., Tavecchio, F., & Dadina, M. 2004, *ApJ*, 600, 634
- Barnes, J. E. & Hernquist, L. 1992, *ARA&A*, 30, 705
- Böker, T., Falcón-Barroso, J., Schinnerer, E., Knapen, J. H., & Ryder, S. 2008, *AJ*, 135, 479
- Bondi, M., Pérez-Torres, M.-A., Dallacasa, D., & Muxlow, T. W. B. 2005, *MNRAS*, 361, 748
- Cappellari, M. & Copin, Y. 2003, *MNRAS*, 342, 345
- Carilli, C. L. & Taylor, G. B. 2000, *ApJ*, 532, L95
- Comerford, J. M., Gerke, B. F., Newman, J. A., Davis, M., Yan, R., Cooper, M. C., Faber, S. M., Koo, D. C., Coil, A. L., Rosario, D. J., & Dutton, A. A. 2009, *ApJ*, 698, 956
- Condon, J. J., Huang, Z.-P., Yin, Q. F., & Thuan, T. X. 1991, *ApJ*, 378, 65
- Davies, R., Engel, H., Hicks, E., Förster Schreiber, N. M., Genzel, R., Tacconi, L. J., Eisenhauer, F., & Rabiën, S. 2010, in *Society of Photo-Optical Instrumentation Engineers (SPIE) Conference Series*, Vol. 7736, *Society of Photo-Optical Instrumentation Engineers (SPIE) Conference Series*
- Davies, R. I., Sternberg, A., Lehnert, M., & Tacconi-Garman, L. E. 2003, *ApJ*, 597, 907
- Do, T., Ghez, A. M., Morris, M. R., Lu, J. R., Matthews, K., Yelda, S., & Larkin, J. 2009, *ApJ*, 703, 1323
- Donley, J. L., Rieke, G. H., Alexander, D. M., Egami, E., & Pérez-González, P. G. 2010, *ApJ*, 719, 1393
- Draine, B. T. & Woods, D. T. 1990, *ApJ*, 363, 464
- Engel, H., Davies, R. I., Genzel, R., Tacconi, L. J., Hicks, E. K. S., Sturm, E., Naab, T., Johansson, P. H., Karl, S. J., Max, C. E., Medling, A., & van der Werf, P. P. 2010, *A&A*, 524, A56
- Farrah, D., Connolly, B., Connolly, N., Spoon, H. W. W., Oliver, S., Prosper, H. B., Armus, L., Houck, J. R., Liddle, A. R., & Desai, V. 2009, *ApJ*, 700, 395
- Ferland, G. J., Korista, K. T., Verner, D. A., Ferguson, J. W., Kingdon, J. B., & Verner, E. M. 1998, *PASP*, 110, 761
- Fu, H., Myers, A. D., Djorgovski, S. G., & Yan, L. 2011, *ApJ*, 733, 103
- García-Marín, M., Colina, L., Arribas, S., & Monreal-Ibero, A. 2009, *A&A*, 505, 1319
- Gerardy, C. L. & Fesen, R. A. 2001, *AJ*, 121, 2781
- Gerke, B. F., Newman, J. A., Lotz, J., Yan, R., Barmby, P., Coil, A. L., Conselice, C. J., Ivison, R. J., Lin, L., Koo, D. C., Nandra, K., Salim, S., Small, T., Weiner, B. J., Cooper, M. C., Davis, M., Faber, S. M., & Guhathakurta, P. 2007, *ApJ*, 660, L23
- Glassman, T. M., Larkin, J. E., & Lafrenière, D. 2002, *ApJ*, 581, 865
- Graham, J. R., Wright, G. S., & Longmore, A. J. 1987, *ApJ*, 313, 847
- Hawarden, T. G., Leggett, S. K., Letawsky, M. B., Ballantyne, D. R., & Casali, M. M. 2001, *MNRAS*, 325, 563
- Heckman, T. M. 1994, in *Mass-Transfer Induced Activity in Galaxies*, ed. I. Shlosman, 234
- Hopkins, P. F. 2012, *MNRAS*, 420, L8
- Hopkins, P. F., Bundy, K., Croton, D., Hernquist, L., Keres, D., Khochfar, S., Stewart, K., Wetzel, A., & Younger, J. D. 2010, *ApJ*, 715, 202
- Hopkins, P. F., Hernquist, L., Cox, T. J., Di Matteo, T., Robertson, B., & Springel, V. 2006, *ApJS*, 163, 1
- Howell, J. H., Armus, L., Mazzarella, J. M., Evans, A. S., Surace, J. A., Sanders, D. B., Petric, A., Appleton, P., Bothun, G., Bridge, C., Chan, B. H. P., Charmandaris, V., Frayer, D. T., Haan, S., Inami, H., Kim, D., Lord, S., Madore, B. F., Melbourne, J., Schulz, B., U, V., Vavilkin, T., Veilleux, S., & Xu, K. 2010, *ApJ*, 715, 572
- Huo, Z. Y., Xia, X. Y., Xue, S. J., Mao, S., & Deng, Z. G. 2004, *ApJ*, 611, 208
- Iwasawa, K., Mazzarella, J. M., Surace, J. A., Sanders, D. B., Armus, L., Evans, A. S., Howell, J. H., Komossa, S., Petric, A., Teng, S. H., U, V., & Veilleux, S. 2011a, *A&A*, 528, A137
- Iwasawa, K., Sanders, D. B., Teng, S. H., U, V., Armus, L., Evans, A. S., Howell, J. H., Komossa, S., Mazzarella, J. M., Petric, A. O., Surace, J. A., Vavilkin, T., Veilleux, S., & Trentham, N. 2011b, *A&A*, 529, A106
- Kennicutt, Jr., R. C. 1998, *ARA&A*, 36, 189
- Klöckner, H.-R. & Baan, W. A. 2004, *A&A*, 419, 887
- Komossa, S., Burwitz, V., Hasinger, G., Predehl, P., Kaastra, J. S., & Ikebe, Y. 2003, *ApJ*, 582, L15
- Koss, M., Mushotzky, R., Treister, E., Veilleux, S., Vasudevan, R., & Trippe, M. 2012, *ApJ*, 746, L22
- Krabbe, A., Gasaway, T., Song, I., Iserlohe, C., Weiss, J., Larkin, J. E., Barczys, M., & Lafreniere, D. 2004, in *Society of Photo-Optical Instrumentation Engineers (SPIE) Conference Series*, Vol. 5492, *Society of Photo-Optical Instrumentation Engineers (SPIE) Conference Series*, ed. A. F. M. Moorwood & M. Iye, 1403-1410
- Krumholz, M. R. & Tan, J. C. 2007, *ApJ*, 654, 304
- Lanz, T. & Hubeny, I. 2003, *ApJS*, 146, 417
- Larkin, J., Barczys, M., Krabbe, A., Adkins, S., Aliado, T., Amico, P., Brims, G., Campbell, R., Canfield, J., Gasaway, T., Honey, A., Iserlohe, C., Johnson, C., Kress, E., LaFreniere, D., Lyke, J., Magnone, K., Magnone, N., McElwain, M., Moon, J., Quirrenbach, A., Skulason, G., Song, I., Spencer, M., Weiss, J., & Wright, S. 2006, in *Society of Photo-Optical Instrumentation Engineers (SPIE) Conference Series*, Vol. 6269, *Society of Photo-Optical Instrumentation Engineers (SPIE) Conference Series*
- Law, D. R., Steidel, C. C., Erb, D. K., Larkin, J. E., Pettini, M., Shapley, A. E., & Wright, S. A. 2009, *ApJ*, 697, 2057
- Liu, X., Shen, Y., Strauss, M. A., & Hao, L. 2011, *ApJ*, 737, 101
- Lutz, D., Veilleux, S., & Genzel, R. 1999, *ApJ*, 517, L13
- Markwardt, C. B. 2009, in *Astronomical Society of the Pacific Conference Series*, Vol. 411, *Astronomical Data Analysis Software and Systems XVIII*, ed. D. A. Bohlender, D. Durand, & P. Dowler, 251
- Max, C. E., Canalizo, G., & de Vries, W. H. 2007, *Science*, 316, 1877
- Mazzarella, J. M., Iwasawa, K., Vavilkin, T., Armus, L., Kim, D.-C., Bothun, G., Evans, A. S., Spoon, H. W. W., Haan, S., Howell, J. H., Lord, S., Marshall, J. A., Ishida, C. M., Xu, C. K., Petric, A., Sanders, D. B., Surace, J. A., Appleton, P., Chan, B. H. P., Frayer, D. T., Inami, H., Khachikian, E. Y., Madore, B. F., Privon, G. C., Sturm, E., U, V., & Veilleux, S. 2012, *AJ*, 144, 125
- McConnell, N. J., Ma, C.-P., Graham, J. R., Gebhardt, K., Lauer, T. R., Wright, S. A., & Richstone, D. O. 2011, *ApJ*, 728, 100
- McGurk, R. C., Max, C. E., Rosario, D. J., Shields, G. A., Smith, K. L., & Wright, S. A. 2011, *ApJ*, 738, L2
- Medling, A. M., Ammons, S. M., Max, C. E., Davies, R. I., Engel, H., & Canalizo, G. 2011, *ApJ*, 743, 32
- Melbourne, J., Ammons, M., Wright, S. A., Metevier, A., Steinbring, E., Max, C., Koo, D. C., Larkin, J. E., & Barczys, M. 2008, *AJ*, 135, 1207
- Melbourne, J., Wright, S. A., Barczys, M., Bouchez, A. H., Chin, J., van Dam, M. A., Hartman, S., Johansson, E., Koo, D. C., Lafon, R., Larkin, J., Le Mignant, D., Lotz, J., Max, C. E., Pennington, D. M., Stomski, P. J., Summers, D., & Wizinowich, P. L. 2005, *ApJ*, 625, L27
- Moré, J. *The Levenberg-Marquardt Algorithm: Implementation and Theory*, Vol. 630 (Berlin: Springer-Verlag), 105
- Mouri, H. 1994, *ApJ*, 427, 777
- Mouri, H., Kawara, K., & Taniguchi, Y. 1993, *ApJ*, 406, 52
- Müller-Sánchez, F., Prieto, M. A., Hicks, E. K. S., Vives-Arias, H., Davies, R. I., Malkan, M., Tacconi, L. J., & Genzel, R. 2011, *ApJ*, 739, 69
- Murray, N. 2009, *ApJ*, 691, 946
- Peng, C. Y., Ho, L. C., Impey, C. D., & Rix, H.-W. 2002, *AJ*, 124, 266
- . 2010, *AJ*, 139, 2097
- Piqueras López, J., Colina, L., Arribas, S., Alonso-Herrero, A., & Bedregal, A. G. 2012, *A&A*, 546, A64
- Pollack, L. K., Max, C. E., & Schneider, G. 2007, *ApJ*, 660, 288
- Ptak, A., Heckman, T., Levenson, N. A., Weaver, K., & Strickland, D. 2003, *ApJ*, 592, 782
- Reunanen, J., Kotilainen, J. K., & Prieto, M. A. 2002, *MNRAS*, 331, 154

- Rich, J. A., Kewley, L. J., & Dopita, M. A. 2011, *ApJ*, 734, 87
- Rich, J. A., Torrey, P., Kewley, L. J., Dopita, M. A., & Rupke, D. S. N. 2012, *ApJ*, 753, 5
- Riffel, R., Rodríguez-Ardila, A., & Pastoriza, M. G. 2006, *A&A*, 457, 61
- Rigopoulou, D., Spoon, H. W. W., Genzel, R., Lutz, D., Moorwood, A. F. M., & Tran, Q. D. 1999, *AJ*, 118, 2625
- Rodríguez-Ardila, A., Pastoriza, M. G., Viegas, S., Sigut, T. A. A., & Pradhan, A. K. 2004, *A&A*, 425, 457
- Rodríguez-Ardila, A., Riffel, R., & Pastoriza, M. G. 2005, *MNRAS*, 364, 1041
- Rosario, D. J., McGurk, R. C., Max, C. E., Shields, G. A., Smith, K. L., & Ammons, S. M. 2011, *ApJ*, 739, 44
- Sanders, D. B. & Mirabel, I. F. 1996, *ARA&A*, 34, 749
- Sanders, D. B., Soifer, B. T., Elias, J. H., Madore, B. F., Matthews, K., Neugebauer, G., & Scoville, N. Z. 1988, *ApJ*, 325, 74
- Scoville, N. Z., Evans, A. S., Thompson, R., Rieke, M., Hines, D. C., Low, F. J., Dinshaw, N., Surace, J. A., & Armus, L. 2000, *AJ*, 119, 991
- Shull, J. M. & Beckwith, S. 1982, *ARA&A*, 20, 163
- Shull, J. M. & Hollenbach, D. J. 1978, *ApJ*, 220, 525
- Smith, H. E., Lonsdale, C. J., & Lonsdale, C. J. 1998, *ApJ*, 492, 137
- Sternberg, A., Hoffmann, T. L., & Pauldrach, A. W. A. 2003, *ApJ*, 599, 1333
- Tadhunter, C. *Optical spectroscopy of Cygnus A: mixed evidence for a hidden quasar* (Cambridge University Press), 33
- Teng, S. H., Schawinski, K., Urry, C. M., Darg, D. W., Kaviraj, S., Oh, K., Bonning, E. W., Cardamone, C. N., Keel, W. C., Lintott, C. J., Simmons, B. D., & Treister, E. 2012, *ApJ*, 753, 165
- Treister, E., Natarajan, P., Sanders, D. B., Urry, C. M., Schawinski, K., & Kartaltepe, J. 2010, *Science*, 328, 600
- van Dam, M. A., Bouchez, A. H., Le Mignant, D., Johansson, E. M., Wizinowich, P. L., Campbell, R. D., Chin, J. C. Y., Hartman, S. K., Lafon, R. E., Stomski, Jr., P. J., & Summers, D. M. 2006, *PASP*, 118, 310
- Van Wassenhove, S., Volonteri, M., Mayer, L., Dotti, M., Bellovary, J., & Callegari, S. 2012, *ApJ*, 748, L7
- Walsh, J. L., van den Bosch, R. C. E., Barth, A. J., & Sarzi, M. 2012, *ApJ*, 753, 79
- Westmoquette, M. S., Clements, D. L., Bendo, G. J., & Khan, S. A. 2012, *MNRAS*, 424, 416
- Wizinowich, P. L., Le Mignant, D., Bouchez, A. H., Campbell, R. D., Chin, J. C. Y., Contos, A. R., van Dam, M. A., Hartman, S. K., Johansson, E. M., Lafon, R. E., Lewis, H., Stomski, P. J., Summers, D. M., Brown, C. G., Danforth, P. M., Max, C. E., & Pennington, D. M. 2006, *PASP*, 118, 297
- Wright, E. L. 2006, *PASP*, 118, 1711
- Wright, S. A., Larkin, J. E., Law, D. R., Steidel, C. C., Shapley, A. E., & Erb, D. K. 2009, *ApJ*, 699, 421
- Xia, X. Y., Xue, S. J., Mao, S., Boller, T., Deng, Z. G., & Wu, H. 2002, *ApJ*, 564, 196
- Younger, J. D., Hayward, C. C., Narayanan, D., Cox, T. J., Hernquist, L., & Jonsson, P. 2009, *MNRAS*, 396, L66